STARS

University of Central Florida
STARS

Electronic Theses and Dissertations, 2004-2019

2010

Correlation Between Preparation Parameters And Properties Of Molybdenum Back Contact Layer For Cigs Thin Film Solar Cells

Eigo Takahashi
University of Central Florida

 Part of the Materials Science and Engineering Commons
Find similar works at: https://stars.library.ucf.edu/etd
University of Central Florida Libraries http://library.ucf.edu

This Masters Thesis (Open Access) is brought to you for free and open access by STARS. It has been accepted for inclusion in Electronic Theses and Dissertations, 2004-2019 by an authorized administrator of STARS. For more information, please contact STARS@ucf.edu.

STARS Citation
Takahashi, Eigo, "Correlation Between Preparation Parameters And Properties Of Molybdenum Back Contact Layer For Cigs Thin Film Solar Cells" (2010). *Electronic Theses and Dissertations, 2004-2019*. 1548.
https://stars.library.ucf.edu/etd/1548

CORRELATION BETWEEN PREPARATION PARAMETERS AND PROPERTIES OF MOLYBDENUM BACK CONTACT LAYER FOR CIGS THIN FILM SOLAR CELLS

by

EIGO TAKAHASHI
B.S. Tohoku University, 2000

A thesis submitted in partial fulfillment of the requirements
for the degree of Master of Science in Materials Science and Engineering
in the Department of Mechanical, Materials and Aerospace Engineering
in the College of Engineering and Computer Science
at the University of Central Florida
Orlando, Florida

Spring Term
2010

©2010 Eigo Takahashi

ABSTRACT

Molybdenum (Mo) thin film back contact layers for thin film $CuIn_{(1-x)}Ga_xSe_2$ (CIGS) solar cells were deposited onto soda lime glass substrates using a direct current (DC) planar magnetron sputtering deposition technique. Requirements for the Mo thin film as a back contact layer for CIGS solar cells are various. Sheet resistance, contact resistance to the CIGS absorber, optical reflectance, surface morphology, and adhesion to the glass substrate are the most important properties that the Mo thin film back contact layer must satisfy.

Experiments were carried out under various combinations of sputtering power and working gas pressure, for it is well known that mechanical, morphological, optical, and electrical property of a sputter-deposited Mo thin film are dependent on these process parameters.

Various properties of each Mo film were measured and discussed. Sheet resistances were measured using a four-point probe equipment and minimum value of 0.25 Ω/sq was obtained for the 0.6 μm-thick Mo film. Average surface roughnesses of each Mo film ranged from 15 to 26 Å were measured by Dektak profilometer which was also employed to measure film thicknesses. Resistivities were calculated from the sheet resistance and film thickness of each film. Minimum resistivity of 11.9 μΩ·cm was obtained with the Mo thin film deposited at 0.1 mTorr and 250 W. A residual stress analysis was conducted with a bending beam technique with very thin glass strips, and maximum tensile stress of 358 MPa was obtained; however, films did not exhibit a compressive stress. Adhesive strengths were examined for all films with a “Scotch-tape” test, and all films showed a good adhesion to the glass substrate.

Sputter-deposited Mo thin films are commonly employed as a back contact layer for CIGS and $CuInSe_2$ (CIS)-based solar cells; however, there are several difficulties in fabricating a qualified back contact layer. Generally, Mo thin films deposited at higher sputtering power and lower working gas pressure tend to exhibit lower resistivity; however, such films have a poor adhesion to the glass substrate. On the other hand, films deposited at lower power and higher gas pressure tend to have a higher resistivity, whereas the films exhibit an excellent adhesion to the glass substrate. Therefore, it has been a practice to employ multi-layered Mo thin film back contact layers to achieve the properties of good adhesion to the glass substrate and low resistivity simultaneously. However, multi layer processes have a lower throughput and higher fabricating cost, and requires more elaborated equipment compared to single layer processes, which are not desirable from the industrial point of view.

As can be seen, above mentioned process parameters and the corresponding Mo thin film properties are at the two extreme ends of the spectrum. Hence experiments were conducted to find out the mechanisms which influence the properties of Mo thin films by changing the two process parameters of working gas pressure and sputtering power individually. The relationships between process parameters and above mentioned properties were studied and explained.

It was found that by selecting the process parameters properly, less resistive, appropriate-surfaced, and highly adhesive single layer Mo thin films for CIGS solar cells can be achieved.

ACKNOWLEDGMENTS

I would like to take this occasion to express my deepest gratitude toward Dr. Neelkanth G. Dhere, for giving me the opportunity to work on this research. I enjoyed working and learning under his supervision, and I appreciate his continuous guidance and encouragement. I would like to appreciate Dr. Aravinda Kar and Dr. Helge Heinrich for serving on my final examination committee and for their invaluable suggestions. AFM measurement was performed at National Renewable Energy Laboratory. Hardness measurement was carried out at University of South Florida. I would like to thank Dr. Sachin Kulkarni, Dr. Vinay Hadagali, and Dr. Parag Vasekar for instructing me the operation of the equipments. I would like to thank Mr. Shirish Pethe, Mr. Ashwani Kaul, and all other colleagues at Florida Solar Energy Center for their collaboration. My research would not have been accomplished without them. I would like to thank KYOCERA Corporation for supporting me in financial and mental aspect. I'm also grateful for Mr. Bihag Joshi and Mr. Saisitaram Ramesh for their cooperation with my work.

I have enjoyed working at PV Materials Laboratory of Florida Solar Energy Center and learning at University of Central Florida. Finally I would like to thank my family and my wife Kozue for their love, understanding and constant support.

TABLE OF CONTENTS

LIST OF FIGURES

LIST OF TABLES

LIST OF ACRONYMS/ABBREVIATIONS/SYMBOLS

ACRONYM/ABBREVIATION/ SYMBOL	Definition
AFM	Atomic Force Microscopy
AM	Air Mass
BCC	Body Centered Cubic
CIS	Copper Indium Diselenide ($CuInSe_2$)
CIGS	Copper Indium Gallium Diselenide ($CuIn_{(1-x)}Ga_xSe_2$)
CIGS2	Copper Indium Gallium Disulfide ($CuIn_{(1-x)}Ga_xS_2$)
CIGSS	Copper Indium Gallium Selenide Sulfide ($CuIn_{(1-x)}Ga_xSe_{(1-y)}S_y$)
DC	Direct Current
e	Electron's Charge (-1.602×10^{-19} C)
E_a	Acceptor Level
E_c	Conduction Band Minima
E_d	Donor Level
E_F	Fermi Level

E_n	Energy Level of Electron
E_{v}	Valence Band Maxima
FF	Fill Factor
FWHM	Full Width at Half Maximum
Gt	Giga Ton (10^{12} kg)
GW	Giga Watt (10^{12} W)
h	Plank Constant (6.626×10^{-34} J·s)
I_0	Reverse Saturation Current
I_{L}	Photo-generated Current
IPCC	Intergovernmental Panel on Climate Change
I_{sc}	Short Circuit Current
i:ZnO	Undoped Zinc Oxide
J_{sc}	Short Circuit Current Density
k	Boltzmann Constant (1.38×10^{-23} J/K)
m_{e}^*	Effective Mass of Electron
m_{h}^*	Effective Mass of Hole

N_A	Acceptor Concentration
N_D	Donor Concentration
n_i	Intrinsic Carrier Concentration
NREL	National Renewable Energy Laboratory
ODC	Ordered Defect Compounds
ppm	Parts Per Million
PV	Photovoltaic
q	Elemental Charge ($+1.602\times10^{-19}$ C)
R_a	Average Roughness
R_s	Series Resistance
R_p	Shunt Resistance
Torr	Torr (133.322 Pa)
V_a	External Voltage
V_B	Built-in Voltage
V_{oc}	Open Circuit Voltage
XRD	X-ray Diffraction

ZnO:Al	Aluminum Doped Zinc Oxide
α	Absorption Coefficient
ε_0	Vacuum Permittivity (8.854×10^{-12} F/m)
ξ	Electric Field
Å	Angstrom (10^{-10} m)

CHAPTER 1 INTRODUCTION

1.1 Need for Renewable Energy

World is facing a severe energy crisis caused by the enormous amount of consumption of fossil fuels such as crude oil, coal, and natural gas. These non-renewable sources of energy were first utilized on a massive scale in the Industrial Revolution in the 18th century. Fossil fuels had been limitlessly consumed until the first oil crisis in 1972 when people realized that oils are not always affordable. Thereafter, people began to research seriously in alternative renewable energy sources such as wind, geothermal heat, tide and waves, hydropower, biomass, and solar power.

Moreover, a number of issues for human beings have been caused by burning fossil fuels to create energy. Global warming, acid rain, and health problems for human lung are typical examples of the problems stem from carbon dioxide and nitrogen oxide emitted by fossil fuel usage. There have emerged so many reasons why we should shift toward renewable energy sources in terms of affordability, environment, and human health, and are described in detail in the following sections.

1.1.1 Renewable Energy

Renewable energies can contribute to meet the global energy demand replacing a large portion of the fossil fuels. As defined in the report of Intergovernmental Panel on Climate Change, “Renewable energy is obtained from the continuing or repetitive currents of energy

occurring in the natural environment and includes non-carbon technologies such as solar energy, hydropower, wind, tide and waves, geothermal heat, as well as carbon-neutral technologies such as biomass (IPCC-WGIII, 2007, p814 (Glossary)).” Renewable energies are also expected to be stable and safe energy sources without negatively affecting the environment.

It is an arduous challenge for us to shift from non-sustainable energies to renewable energies as main energy sources because there are still a number of barriers to be overcome. However, with technological progresses, political and economical alignments, renewable energies have great potentials to dominate the energy sector across the world.

1.1.2 Global Energy Market Crisis

The primary energy demand throughout the world is predicted to increase by 1.5% every year. It will increase from 12 giga ton (Gt) in 2007 to 16.8 Gt in 2030 in terms of petroleum, which amounts up to 40% of increase [1]. Although the world’s energy consumption decreased in 2009 for the first time since 1981 due to the global recession in recent years [1], it is obvious that massive global energy consumption would proceed again once the economy recovers from this slump.

Ever since fossil fuels became the world’s primary energy sources, there have been wild swings in the price of oil, coal, and natural gas. It has been shown that the oil price has the strong correlation with the world’s both economic and industrial condition. In other words, it is expected that the price of oil will increase in accordance with the recovery of the world’s economy and industrial demands. This correlation is totally unfavorable especially for

developing countries because the expensive energy source should suppress their economic activities and impede them from growing steadily.

1.1.3 Depletion of Fossil Energy Sources

For the rapid development of technology, it is essential to have an abundant source of energy which has been the case for so many years with the fossil fuel being the primary energy source. However, the amount of fossil fuels is limited, and it is predicted that the crude oil will be depleted in 40 years and the coal will be depleted in 200 years at the longest [2]. Hence, for the further industrial and technological development, it is necessary to develop a suitable replacement for fossil fuels that is efficient in producing the same amount of energy.

1.1.4 Global Climate and Health Threat

In the last decade, there has been a dramatic rise in global warming due to the greenhouse effect, which potentially harms creatures on earth. Global warming seems to have caused melting of the ice belt in the North and South Pole area, heat waves, hurricanes, and flooding across the world. The IPCC predicted that, by 22nd century, the earth's sea level will become tens of centimeters higher and the average temperature will be several degrees Celsius higher than that of today [3].

The global warming is assumed to be caused by greenhouse gases (GHGs) such as carbon dioxide (CO_2) and nitrogen oxide (NO_x) which are exhausted by burning fossil fuels to create motivities or operating thermal power plants to create electric energies. The CO_2 emission had

already increased from 20.9 Gt in 1990 to 28.8 Gt in 2007, and forecasted to increase by 1.5% per year in average and consequently approach 34.5 Gt in 2020 [1]. The atmospheric CO_2 concentration used to be approximately 280 ppm before the Industrial Revolution; however, it is 380 ppm today [3].

In addition to the environmental damage, the operation of thermal power plants also negatively affects human health. A large amount of air pollution generated by fossil fuel burning is affecting air quality and human health [4].

1.2 Photovoltaic Solar Cell

Among all the renewable energy technologies, one of the most promising technologies is the photovoltaic (PV) solar energy system which can convert sunlight directly into electric power emitting neither greenhouse gases nor pollutants, and requiring no power supply for its operation [5]. PV solar energy systems are also simply mentioned as solar cells. In 2008, the global annual PV market reached 5.6 giga Watt (GW) and the cumulative PV power installation amounted to almost 15 GW as shown in Figures 1-1 and 1-2 [6]. Until 2013, European Photovoltaic Industry Association (EPIA) expects the global annual PV market to increase up to 22 GW with governmental supports.

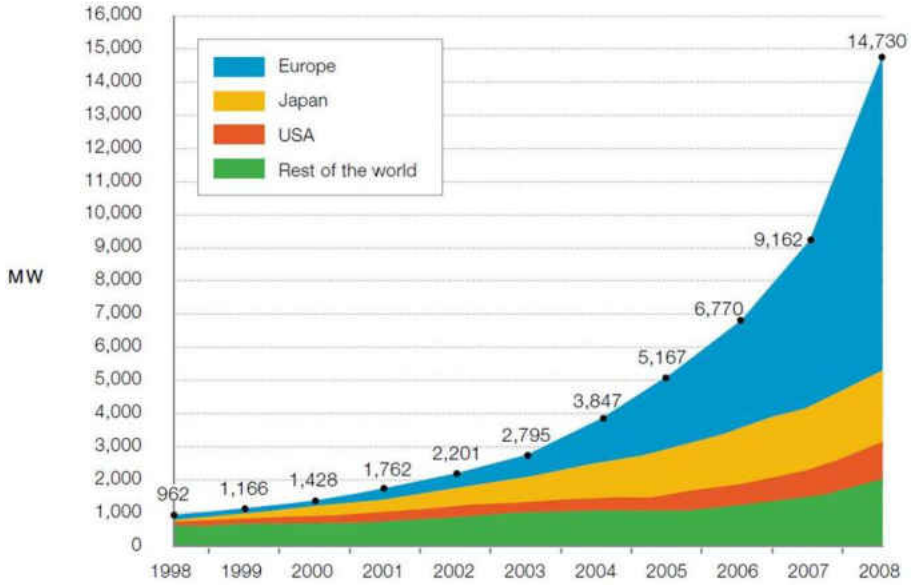

Figure 1-1: Historical development of Global cumulative PV power installed per Region [6]

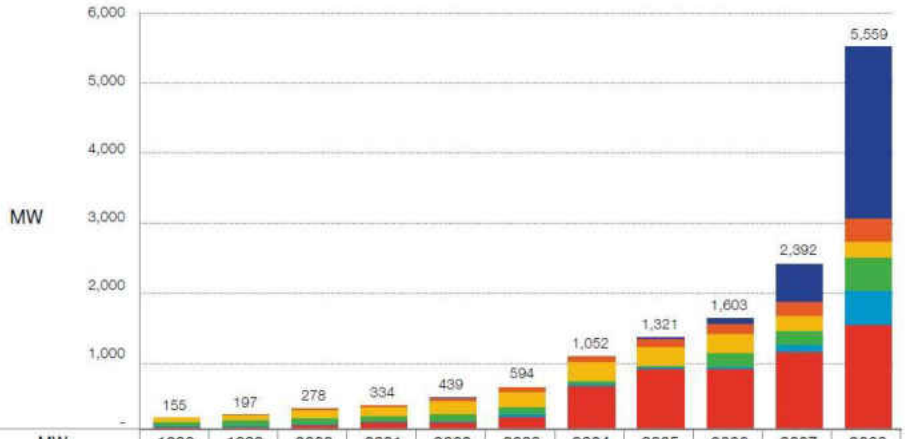

MW	1998	1999	2000	2001	2002	2003	2004	2005	2006	2007	2008
Spain	0	1	-	2	9	10	6	26	88	560	2,511
USA	-	17	22	29	44	63	90	114	145	207	342
Japan	69	72	112	135	185	223	272	290	287	210	230
Rest of the world	68	84	94	75	104	98	53	12	196	207	485
Rest of Europe	8	11	10	16	16	50	30	30	37	108	492
Germany	10	12	40	78	80	150	600	850	850	1,100	1,500
TOTAL	155	197	278	334	439	594	1,052	1,321	1,603	2,392	5,559

Figure 1-2: Historical development of Global annual PV market per region [6]

1.2.1 Advantages of Solar Cell

One of the largest advantages of PV solar energy system is its broad option for the location to install due to the omnipresence of sunlight. Moreover, since PV systems emit neither greenhouse gases, toxic gases, nor pollutants during the operation, it is possible to install PV system in any available space even in the middle of thickly inhabited cities without putting the residents' health at risk [7]. Thus, PV system is suitable for distributed power source. As a matter of fact, 66 % of the world's installation today is on roof-tops of home units or buildings [8].

Another advantage of solar cells is that they are long lasting steady energy sources. Although it requires expensive cost for the initial installation, once it has installed, very little maintenance is required during the operating lifetime approximately 20 years.

Owing to its advantages, PV systems can be designed for wide variety of applications such as water pumping, lighting, vehicle, portable electric device, heat exchanger system, remote village electrification, and grid-connected power source [7]. A number of solar power plants have already started their operation across the world.

1.2.2 Drawbacks of Solar Cell

Although PV solar systems require no fuel and very little maintenance with long time reliability, the initial investment is quite expensive to popularize them rapidly. The technical potential of solar cells has been well investigated but there are questions if PV systems can economically compete with conventional grid electricity generating systems such as thermal power plant. Innovative researches have shown more than 20% of energy conversion efficiencies

of solar cells; however, further technical development or new technology is necessary to meet the expectation as the substitution for fossil energy sources.

1.3 CIGS Solar Cell

The investigations in PV industry as well as research institutes are mainly focused on the development of highly efficient materials which can be manufactured with inexpensive processes to reduce the production cost with respect to the energy conversion performance. From such an industrial point of view, thin film solar cells are referred to as second generation solar cells. Namely, the thin film solar cell technology has been developed to reduce the manufacturing cost of PV systems by reducing the raw material usage, simplifying the process, and developing the yield and throughput.

Among the variety of materials used for thin film solar cells, $CuIn_{(1-x)}Ga_xSe_2$ (CIGS) absorber based heterojunction solar cell has the largest potential as to cost reduction with respect to power generation efficiency. The reported highest efficiencies of CIGS solar cell and module are 20% and 16.7% respectively [9], [10].

1.4 Molybdenum Back Contact Layer

Various criteria need to be satisfied for a choice of high quality back contact thin film layer for CIGS solar cells. It is a prerequisite to be unreactive with adjoining CIGS absorber

layer to avid degradation of the absorber and achieve reproducible fabrication. However, this requirement is quite a high hurdle because of the erodent environment during the growth of CIGS layer. Conductivity and adherence to the substrate should also be maintained throughout the fabrication process and expected operating lifetime. Another important criterion for a back contact layer is that it has to play a role as barrier layer that interrupts harmful elements' diffusion from the substrate into the CIGS absorber layer. A high optical reflectance is also required to avoid optical loss.

A variety of investigation has been conducted on potential metal thin film back contact layers including Mo [11], [12], [13], Pt [12], [13], [14], Au [13], [15], [16], Ni [16], [17] and Cu [15]. Among all these materials, Mo is the most befitted material for a back contact thin film layer for CIGS solar cells. Mo is chemically stable against Cu, In, Ga, and their alloys during the fabrication process; it also shows low Ohmic contact resistance to CIGS absorber via an intermediate molybdenum diselenide ($MoSe_2$) layer [18]. CIGS based solar cells have been reported as most efficient thin film solar cells with a Mo back contact layer. The highest efficient CIGS solar cell was also deposited on a Mo back contact layer [9]. A number of investigations have reported about the correlations between mechanical, optical, and electrical properties of Mo thin films and process parameters of direct current (DC) magnetron sputtering technique [11].

It is well known that sputter-deposited Mo thin films have a correlation between working gas pressure and residual stress, which is typically observed in refractory metals [19], [20], [21], [22]. It has also been reported that sputtering power influences stress state of the Mo thin films. Other investigations have reported adherence to glass substrate and electrical resistivity of the

Mo thin films are strongly dependent on the working gas pressure [11], [19], [22], [23], [24], [25]. As just described, Mo thin film can possess a variety of properties by varying the process parameters. For example, films deposited at lower working gas pressures generally have poor adherence to the substrate, low resistivity, and compressive stress state, whereas those deposited at higher gas pressures tend to have good adherence, high resistivity, and tensile stress state. Note that the measure for high and low pressure or power is uniquely dependent on each individual sputtering system. A number of investigations have reported the influences of working gas pressure on the mechanical and electrical properties of Mo thin film back contact layers as well as their eventual effects on the performances as a solar cell [11], [19], [22], [26], [27]. To control the stresses residing in the thin films is vital to their long lifetime, reliability, and high performance as a back contact layer of CIGS solar cells [28].

1.5 Literature Review

One of the main factors which influence the film's adherence is residual stress. B.C. Bell *et al*. reported that film stress was strongly dependent on working gas pressure and angle of sputtered atom incidence [28]. Similar result was reported by J.H. Scofield *et al*. who showed that films in compressive stress state had poor adherence and those in tensile stress had good adherence to the glass substrate [11]. Y.G. Shen reported that Mo films' stresses drastically change the stress state from tensile to compressive in the vicinity of the transition pressure ranging from 8 to 10 mTorr [29], while D.W. Hoffman *et al*. obtained the transition pressure

around 0.2 mTorr [20]. Shen also mentioned that compressive films are densely packed microstructure, and tensile films have a very porous columnar microstructure.

Difference in microstructure originated from the working gas pressure directly influences the resistivity of the films. G. Gordillo *et al*. showed that the resistivity of sputter-deposited Mo thin film is highly influenced by both target power and working gas pressure [30]. J.H. Scofield *et al*. investigated that the resistivity of about 10μΩ·cm was steadily obtained at pressures between 0.2 and 2 mTorr without significant pressure dependence, followed by steep increase at pressure of more than 2 mTorr [11].

Previous reports have also shown that it is very difficult to achieve a well adherent and low resistive single Mo thin film layer [11], despite the fact that both characteristics are essential for stable and highly efficient solar cell fabrication. In order to break through this problem, multi-layered Mo film is widely used. For example, National Renewable Energy Laboratory (NREL) has achieved highly adhesive and conductive Mo thin films by varying process parameter such as working gas pressure during the deposition [11], [18]. They deposited a good adherent but poor conductive Mo thin film as an initial layer on the glass substrate to glue the following layer to the glass substrate. Then low resistive Mo thin film was deposited over the initial “glue” layer, and consequently they obtained good adhesive and conductive two-layered Mo thin film. Some other groups deposit more than 2 layers to enhance the adherence and conductivity.

1.6 Motivation of the Study

As mentioned above, multi-layered Mo thin film layer is widely used to achieve good adhesion and conductivity simultaneously. However, because this multi layer process requires several deposition steps and specialized equipment, it is not an ideal process in terms of both time and cost.

The motivation of this investigation is to find out how DC magnetron sputtering deposition system parameters such as working gas pressure and sputtering power influence the properties of Mo thin film layers and the performances of CIGS solar cells, and eventually achieve a qualified Mo thin film single layer.

CHAPTER 2 BASICS OF SOLAR CELL

2.1 History

A solar cell is a device that can directly convert the light energy into the electricity through the photovoltaic effect. The first development of solar cell technology began with photoelectric effect discovered by French physicist Antoine César Becquerel in 1839. However, the early solar cells could achieve energy conversion efficiencies of below 1% until Russell Ohl invented the silicon solar cell in 1940s. Since Ohl's invention of silicon solar cell, researches in this field have been focused on silicon based solar cells and the highest efficiency of 25% has been achieved in silicon single crystal solar cell by J. Zhao *et al*. [31].

2.2 Solar Radiation

In solar energy field, air mass (AM) is one of the most important factors in characterizing a solar cell. AM is the relative optical path length through the earth's atmosphere with respect to the normal incidence from a source in space. When the light source is right above the observer, the air mass is unity. Since fine particles and gas molecules floating in the earth's atmosphere are the scattering and absorption sites for lights, the longer a light passes through the atmosphere, the greater the attenuation become. In outer space, namely if there is no atmospheric attenuation, the

radiation intensity from the sun, or the solar constant is 1353 W/m^2, and is referred to as AM0 (air mass zero) radiation.

The path length T through the earth's atmosphere for a radiation from the sun incident at an angle ϕ relative to the normal to the earth's surface (see Figure 2-1) is given by

$$T = T_0 \sec\phi \qquad \cdots\cdots\cdots (2.1)$$

where T_0 is the thickness of the atmosphere. The air mass is simply given by the secant of the zenith angle, ϕ.

$$\frac{T}{T_0} = AM = \sec\phi \qquad \cdots\cdots\cdots (2.2)$$

The standard evaluation of a solar cell's performance is evaluated with AM1.5 radiation corresponding to the solar constant of 1000 W/m^2. The solar constant on the earth's ground surface is always lower than that in outer space due to the spectral absorption and scattering by the atmospheric fine particles, water vapor, carbon dioxide, and other gas molecules. The easiest way to calculate AM value at different location on earth is given by,

$$\text{AM} = \sqrt{1 + \left(\frac{S}{H}\right)^2} \qquad \cdots\cdots\cdots (2.3)$$

where S is the length of the shadow cast by a vertical object of height H.

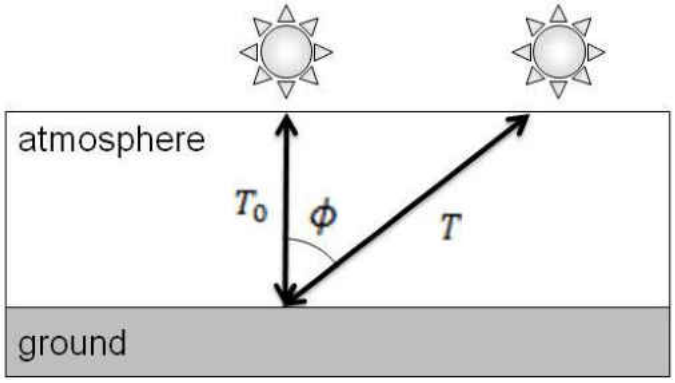

Figure 2-1: Schematic image of air mass

2.3 Semiconductor

A solar cell is a simple p-n junction diode if there is no light falling on the cell. In other words, a solar cell is a p-n junction diode that can produce electric power when light is incident on it. This particular characteristic makes a solar cell one of the most useful renewable energy sources because one can produce electric power using abundantly available sunlight. Therefore, it is essential to be familiar with basic knowledge of semiconductors to understand the function of solar cells. In this section, silicon is picked up as an example of semiconductor material because it is a single element semiconductor and suitable to obtain basic knowledge.

2.3.1 Energy State of Electron

An electron in free space can arbitrarily have an energy value that it can attain. However, the situation in an atomic orbit or in a crystal is quite different [32]. An atom in an isolated space

is electrically neutral because the positive charge of the nucleus is compensated by the negatively charged orbital electrons. The electrons in an atom are acted upon by an electromagnetic field exerted by the nucleus and electrons themselves, letting electrons posses a certain allowed energy. An electron orbiting an isolated atom can occupy one of the series of energy levels, E_{n} given by the following approximate equation [33],

$$E_n = -\frac{Z^2 m_{\mathrm{e}}^* e^4}{8\varepsilon_0^2 h^2 n^2} \qquad \cdots\cdots\cdots (2.4)$$

where e is the charge of an electron, Z is the atomic number, m_{e}^* is the mass of a free electron, ε_0 is the vacuum permittivity, h is the Plank constant and n is a positive integer representing energy levels. At equilibrium, not all the electrons can occupy the lowest energy level at the same time. According to Pauli's exclusion principle, at most two electrons can reside in the same energy level by acquiring opposite spin direction. These energy levels are further constructed in shell structures governed by four quantum numbers given by classical quantum theory.

2.3.2 Forbidden Energy Gap

When atoms are located in a free space, an electron in each individual atom occupies one of the energy levels given by equation (2.4). However, as several atoms are brought closer, atoms begin to exert force one another with disturbing the potential and the energy levels of the electron consequently. When two atoms from the same element are brought closer, the energy level of E_n occupied by two electrons in each atom cannot accommodate the four electrons as it violates the Pauli's exclusion principle. To avoid violating the principle, the energy level E_n

becomes disturbed and splits into two slightly separated energy levels. If N atoms are brought together to construct a crystal, they interact and the original energy level E_n is split into N slightly different allowed energy levels to accommodate $2N$ numbers of electrons. Figure 2-2 shows the case where the atomic spacing, d is such that the material has two energy bands separated by the forbidden energy gap. Hereafter, band structure will be represented by two lines indicating valence band maxima and conduction band minima separated by band gap.

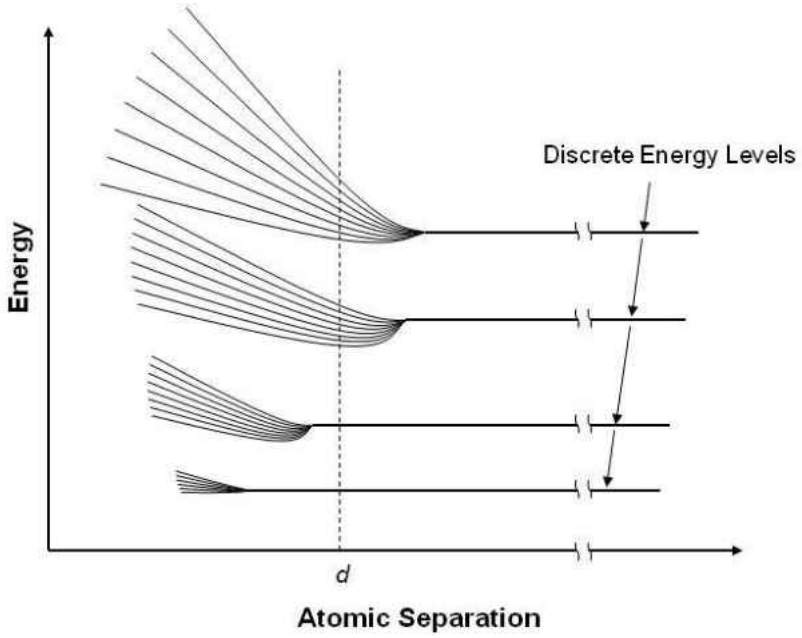

Figure 2-2: Split energy levels of electron when atoms are brought closer (redrawn form [32])

2.3.3 Electron Distribution in Semiconductor

The valence band is completely filled by electrons while the conduction band is completely empty if the temperature is 0 K. As the temperature increases, some of the electrons gain enough energy to leap the forbidden gap and enter the conduction band. The effect of temperature on the occupancy of electrons in each allowed energy level E is given by the Fermi-Dirac distribution function $f(E)$ [33],

$$f(E) = \frac{1}{\exp\left(\frac{E - E_{\mathrm{F}}}{kT}\right) + 1} \qquad \cdots\cdots\cdots (2.5)$$

where k is the Boltzmann constant, T is the absolute temperature, and E_{F} is the Fermi level. The Fermi-Dirac distribution function determines the probability of electron occupancy at any given energy, E at temperature, T. Fermi level is defined as the highest energy level occupied by electrons at absolute zero temperature. It is also defined as the energy level where the probability of charge carrier occupancy is 50%. Those materials which have E_{F} within an allowed energy band are called metal. Insulators have a large band gap between the valence and conduction bands so that electrons cannot leap across. A semiconductor can be defined as just an insulator with a narrow band gap. For an intrinsic semiconductor, Fermi level is at the center of the forbidden gap.

2.3.4 Electrical Properties

In silicon, p-type semiconductor is obtained by doping with an element from the group III as an acceptor such as boron (B) or aluminum (Al), and n-type is obtained with an element from

the group V as a donor such as phosphorous (P). Whereas some compound semiconductors such as copper chalcopyrite material can produce acceptors or donors inherently as they crystallize. Point defects such as vacancies, interstitials and antisites are responsible for the electric characteristics of copper chalcopyrite semiconductors.

The majority carrier in p-type semiconductor is hole, while electron is the majority carrier in n-type semiconductor. By doping a semiconductor with donor elements, an additional energy level slightly below the conduction band is introduced by electrons freed from the donor impurities. For instance, addition of phosphorous as a donor impurity in silicon semiconductor introduces an energy level called donor level, E_{d} which is 0.045 eV below the conduction band. The value of 0.045 eV is comparable with thermal energy at room temperature of about kT = 0.026 [eV], and as a matter of fact, the donors are well ionized at room temperature. At low temperature, E_{F} lies between the conduction band edge and E_{d}. However, at room temperature, the number of ionized donors is significant so that a number of electrons occupy the conduction band, E_{F} shifts towards the intrinsic Fermi level. Eventually, E_{F} lies in between intrinsic Fermi level and E_{d}. Similarly, with the addition of acceptors, the Fermi level in p-type semiconductor resides between acceptor level, E_{a} and intrinsic Fermi level.

At high energy levels such that $E - E_{\mathrm{F}} \gg kT$, the Fermi-Dirac function ban be substituted by the Boltzmann function given by [33].

$$f(E) = \exp\left[\frac{-(E - E_{\mathrm{F}})}{kT}\right] \qquad \cdots\cdots\cdots (2.6)$$

The probability of electron existing in the forbidden gap is zero, while it is nonzero in the allowed energy bands. The number of states per unit volume and energy is given by solving the time-independent Schrödinger equation. The density of states at energy E near the conduction band edge is given by [34]

$$g_{\mathrm{c}}(E) = \frac{m_{\mathrm{e}}^{*}\sqrt{2m_{\mathrm{e}}^{*}(E - E_{\mathrm{c}})}}{\pi^{2}h^{3}} \qquad \cdots\cdots\cdots (2.7)$$

Similarly, density of states at energy E near the valence band edge is given by [34]

$$g_{\mathrm{v}}(E) = \frac{m_{\mathrm{h}}^{*}\sqrt{2m_{\mathrm{h}}^{*}(E_{\mathrm{v}} - E)}}{\pi^{2}h^{3}} \qquad \cdots\cdots\cdots (2.8)$$

, where m_{e}^{*} is effective mass of electron, m_{h}^{*} is effective mass of hole, $E_{\mathrm{c}}$is the conduction band minima, and E_{v} is the valence band maxima. The carrier concentration is the product of probability of occupancy and the number density of available states. Therefore, electron concentration in the conduction band can be written as [33]

$$n_{0} = \int_{E_{\mathrm{c}}}^{\infty} g_{\mathrm{c}}(E) f(E) dE \qquad \cdots\cdots\cdots (2.9)$$

By substituting equations (2.6) and (2.7) into equation (2.9), we obtain [33]

$$n_{0} = N_{\mathrm{c}} \exp\left(\frac{E_{\mathrm{F}} - E_{\mathrm{c}}}{kT}\right) \qquad \cdots\cdots\cdots (2.10)$$

where n_0 is the electron number density in the conduction band, N_{c} is a constant at fixed temperature known as effective density of states in the conduction band given by

$$N_c = 2\left(\frac{2\pi m_e^* kT}{h^2}\right)^{3/2} \qquad \cdots\cdots\cdots (2.11)$$

Similarly, the hole number density in the valence band p_0 is obtained by [33]

$$p_0 = \int_{-\infty}^{E_v} g_v(E)[1 - f(E)]dE \qquad \cdots\cdots\cdots (2.12)$$

$$p_0 = N_v \exp\left(\frac{E_v - E_F}{kT}\right) \qquad \cdots\cdots\cdots (2.13)$$

$$N_v = 2\left(\frac{2\pi m_h^* kT}{h^2}\right)^{3/2} \qquad \cdots\cdots\cdots (2.14)$$

where N_v is a constant at fixed temperature known as effective density of states in the valence band. The schematic explanation for the concentrations of electron and hole for intrinsic, n-type, and p-type semiconductors are shown in Figures 2-3, 2-4, and 2-5 respectively.

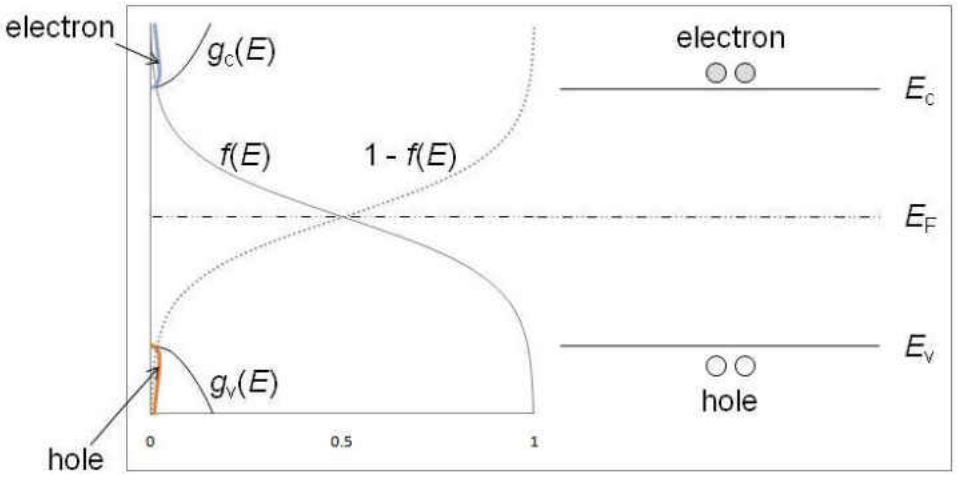

Figure 2-3: Carrier occupancy in valence band and conduction band in case of intrinsic semiconductor

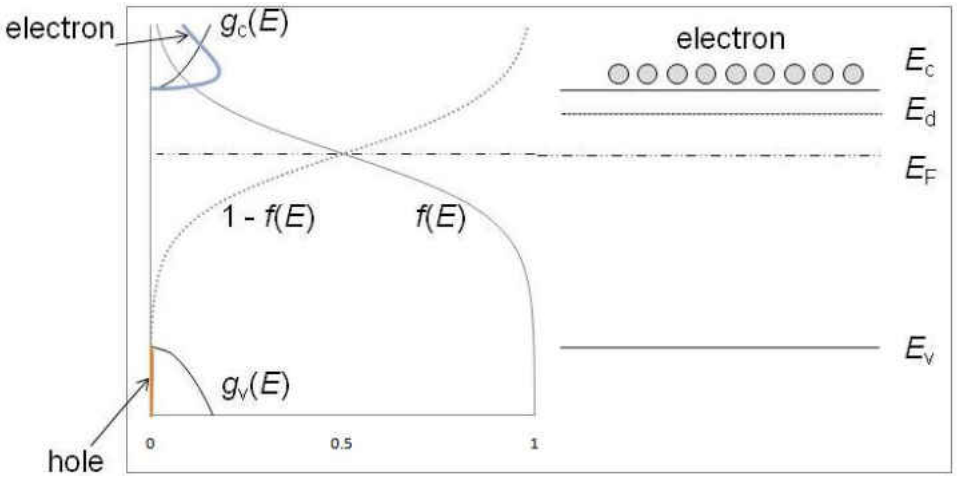

Figure 2-4: Carrier occupancy in valence band and conduction band in case of n-type semiconductor

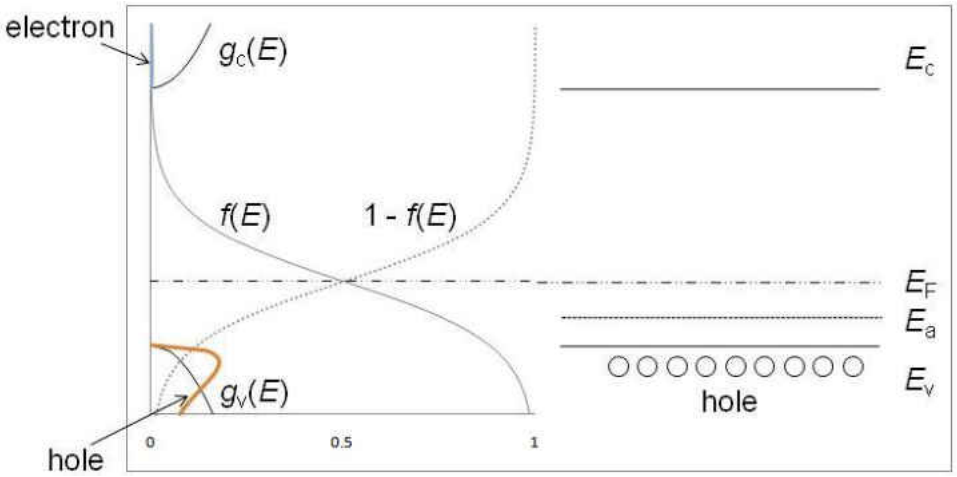

Figure 2-5: Carrier occupancy in valence band and conduction band in case of p-type semiconductor

2.4 p-n Junction

When p-type and n-type semiconductors are brought together, thermal equilibrium of individual system is broken and re-establishment of the new thermal equilibrium for the conjunct system occurs. Namely, electrons from n-type semiconductor migrate into the p-type semiconductor to fill in the holes. However, as these carriers move across to the opposite side of material, they leave behind electrically uncompensated dopant ions. Since these ions are not capable of moving, the migration of carriers eventually set up an electric field across the junction where negative ions reside in p-type side and positive ions are in n-type side. Different from bulk domain, charge carriers cannot reside within this built-in electric field but immediately drift away, therefore this region is called depletion region. This built-in electric field opposes the natural diffusion tendency of carriers and equilibrium is obtained. It is this potential that drives the photo-generated electrons to the external circuit (See Figure 2-6).

The product of current and voltage yields the power that can be used to run varied applications. It is obvious that current is zero at equilibrium. At this condition the electric field, ξ established by diffusion of charge carriers is given by

$$\xi = \frac{kT}{e}\frac{1}{n}\frac{dn}{dx} \qquad \cdots\cdots\cdots (2.15)$$

where n is the free electron concentration at equilibrium. Note that the electric field is maximum at the junction. The built-in voltage V_B is the integration of the electric field from p-side to n-side [34].

$$V_{\mathrm{B}} = -\int_{\text{p-side}}^{\text{n-side}} \xi dx \qquad \cdots\cdots\cdots (2.16)$$

On solving the integral

$$V_{\mathrm{B}} = \frac{kT}{q} \ln \frac{N_{\mathrm{A}} N_{\mathrm{D}}}{n_{\mathrm{i}}^2} \qquad \cdots\cdots\cdots (2.17)$$

where q is the elemental charge, N_{A}, N_{D}, and n_{i} are the acceptor, donor, and the intrinsic carrier concentration, respectively.

The width of depletion region W is dependent on the dopant concentration and the built-in voltage and applied voltage. At equilibrium condition, the applied bias is zero; therefore, the depletion width is determined only by the built-in voltage given by [34].

$$W = W_{\mathrm{n}} + W_{\mathrm{p}} = \sqrt{\frac{2\varepsilon_{\mathrm{s}} V_{\mathrm{B}} (N_{\mathrm{A}} + N_{\mathrm{D}})}{q N_{\mathrm{A}} N_{\mathrm{D}}}} \qquad \cdots\cdots\cdots (2.18)$$

where W_{n} is depletion width in n-type material, W_{p} is depletion width on p-type material, and ε_{s} is permittivity of the material. When an external voltage V_{a} is applied, the depletion width is modified as [34]

$$W = \sqrt{\frac{2\varepsilon_{\mathrm{s}} (V_{\mathrm{B}} - V_{\mathrm{a}}) (N_{\mathrm{A}} + N_{\mathrm{D}})}{q N_{\mathrm{A}} N_{\mathrm{D}}}} \qquad \cdots\cdots\cdots (2.19)$$

The depletion width increases in the reverse biased condition ($V_{\mathrm{a}} < 0$), while W decreases in forward biased condition ($V_{\mathrm{a}} > 0$). A forward bias results in a reduction of the potential barrier

across the junction making it easier for majority charge carriers to cross over to the opposite regions and recombine.

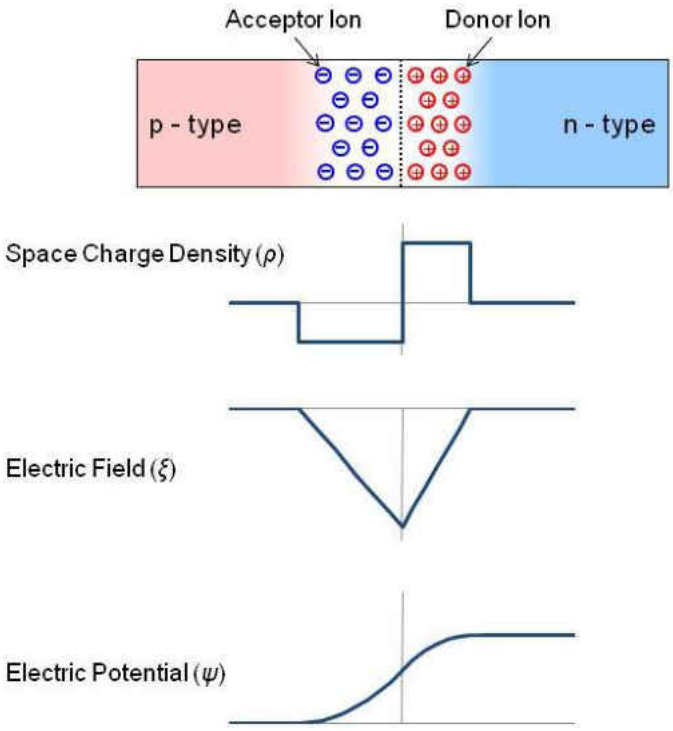

Figure 2-6: Schematic image of p-n junction and corresponding space charge density, electric field, and electric potential across the p-n junction

2.5 Heterojunction

The physics of semiconductor discussed so far was related to homojunction. However, CIGS/CdS is a heterojunction device; hence it is important to understand the additional features

involved in the band diagram. Heterojunction has a potential of improving the performance of solar cells. A heterojunction is the interface between two different semiconductor materials such as p-type CIGS and n-type CdS as shown in Figure 2-7, where the numbers represent each material: (1) $MoSe_2$, (2) CIGS, (3) CdS, and (4) ZnO, and the subscripts "c" and "v" denote conduction and valence band, respectively.

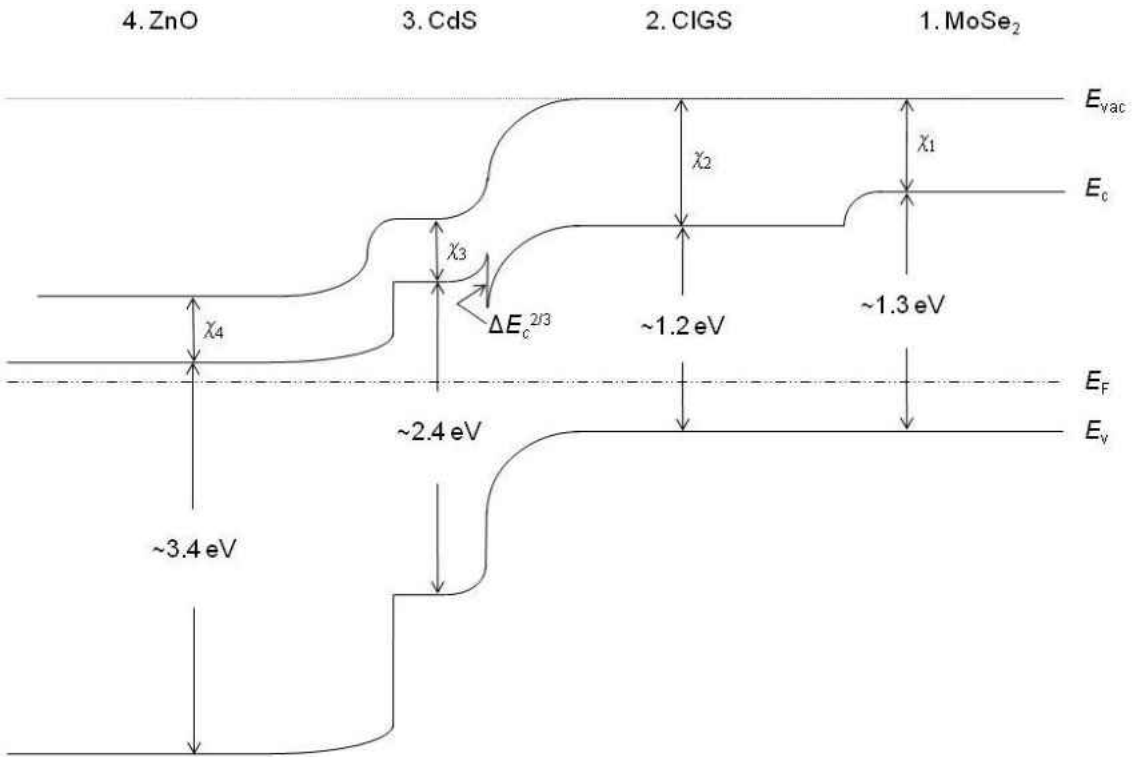

Figure 2-7: Heterogeneous band diagram of ZnO/CdS/CIGS/Mo solar cell

In the case of heterojunction system, each material has its own value of band gap, electron affinity χ, and work function Φ, and they are different from each other. Therefore, band

offset of the adjacent semiconductors, ΔE is developed. For the vacuum level to remain continuous at the interface, a discontinuity necessarily occurs in the conduction band as well as valence band. The discontinuity of the conduction band between CIGS and CdS layer is described as [33]

$$\Delta E_{\mathrm{c}}^{2/3} = \chi_2 - \chi_3 \qquad \cdots\cdots\cdots (2.20)$$

The discontinuities at the interface affect the space charge storage in the adjacent regions. In the neutral region, away from the interface, the relationship between the conduction band edge of CdS and the Fermi level is determined by [33]

$$E_{\mathrm{c3}} - E_{\mathrm{F}} = kT \ln\left(\frac{N_{\mathrm{C3}}}{N_{\mathrm{D3}}}\right) \qquad \cdots\cdots\cdots (2.21)$$

where N_{C3} is the effective density of state in the conduction band, and N_{D3} is the donor density of the CdS layer. In the case of CIGS, it is given by

$$E_{\mathrm{c2}} - E_{\mathrm{F}} = E_{\mathrm{g2}} - (E_{\mathrm{F}} - E_{\mathrm{v2}}) = E_{\mathrm{g2}} - kT \ln\left(\frac{N_{\mathrm{V2}}}{N_{\mathrm{A2}}}\right) \qquad \cdots\cdots (2.22)$$

where N_{V2} is the effective density of state in valence band, and N_{A2} is the acceptor density of the CIGS layer. Hence, the gap in the conduction band edge in the neutral region is independent of electron affinities and is written as [33]

$$E_{\mathrm{c2}} - E_{\mathrm{c3}} = E_{\mathrm{g2}} - kT \ln\left(\frac{N_{\mathrm{C3}} N_{\mathrm{V2}}}{N_{\mathrm{D3}} N_{\mathrm{A2}}}\right) \qquad \cdots\cdots\cdots (2.23)$$

To hold the same value of $E_{c2} - E_{c3}$ between the neutral regions with positive non-zero ΔE_c⅔ at the interface, the total bending of the energy bands must increase by ΔE_c⅔. The built-in potential also increases with positive ΔE_c⅔ as the individual work function Φ_2 and Φ_3 changes. The greater bending of the energy bands with different electron affinities implies that the depletion region widens and hence the V_{oc}. The importance of the spike as a barrier to the electron flow from n-type to p-type depends on the fraction of the built-in potential dropped on each side. If the acceptor concentration in p-type material is low as compared to the donor concentration in the n-type material, the majority of band bending occurs in the p-type material side and the top of the spike is lower than the conduction band edge in the neutral region of the p-type material. The barrier to electron flow from n-type to p-type is then just the difference in the conduction band edges in the neutral region of the two materials. However, if the doping in the p-type material is higher compared to the n-type material then the majority of band bending occurs in the n-type material and the top of spike can be higher than the conduction band edge in the neutral region of the p-type material. In this case the barrier to electron flow n to p type is greatly increased.

2.6 Current Voltage Characteristics

2.6.1 Carrier Injection

A solar cell is a simple p-n junction diode under no illumination. When forward bias is applied to the diode, excess electrons in the n-type are injected into the p-type region across the interface, while excess holes are injected into the n-type region. Applying a forward bias results

in a reduction of the potential barrier across the junction, and it also makes it possible for charge carriers to flow to the opposite side of the interface. It is mathematically implicated that the minority carrier concentration increases exponentially with applied voltage; however, the lifetime of them are short in neutral region due to the high recombination rate. Therefore, the relationship is only valid within the depletion region [33]. Note that the minority carrier in p-type semiconductor is free electron and that of n-type semiconductor is hole.

$$n_{\mathrm{pw}} = n_{\mathrm{p0}} \exp\left(\frac{qV_{\mathrm{a}}}{kT}\right) \qquad \cdots\cdots\cdots (2.24)$$

$$p_{\mathrm{nw}} = p_{\mathrm{n0}} \exp\left(\frac{qV_{\mathrm{a}}}{kT}\right) \qquad \cdots\cdots\cdots (2.25)$$

where n_{pw} is the injected minority carrier concentration at the depletion region interface of the p-type side, n_{p0} is the minority carrier concentration at thermal equilibrium, p_{nw} is the injected minority carrier concentration at the depletion region interface of the n-type side, p_{n0} is the minority carrier concentration at thermal equilibrium.

2.6.2 Diffusive Flow

The excess minority carrier concentration decreases exponentially with the distance away from the depletion region edge as shown in Figure 2-8. The concentration of the minority carriers are given by [33]

$$\hat{n} = n_{\mathrm{pw}} \exp\left(\frac{-x}{\sqrt{D_{\mathrm{n}}\tau_{\mathrm{n}}}}\right) \qquad \cdots\cdots\cdots (2.26)$$

$$\hat{p} = p_{\mathrm{nw}} \exp\left(\frac{-x}{\sqrt{D_{\mathrm{p}}\tau_{\mathrm{p}}}}\right) \qquad \cdots\cdots\cdots (2.27)$$

where D_{n} and D_{p} are the diffusion coefficients of electron and hole minority carriers, τ_{n} and τ_{p} are the lifetime of electron and hole minority carriers, respectively. $\hat{n}$ is the injected minority carrier concentration in p-type region, $\hat{p}$ is the injected minority carrier concentration in n-type region as shown in Figure 2-8. Note that the x axes in equation (2.26) and (2.27) are defined differently.

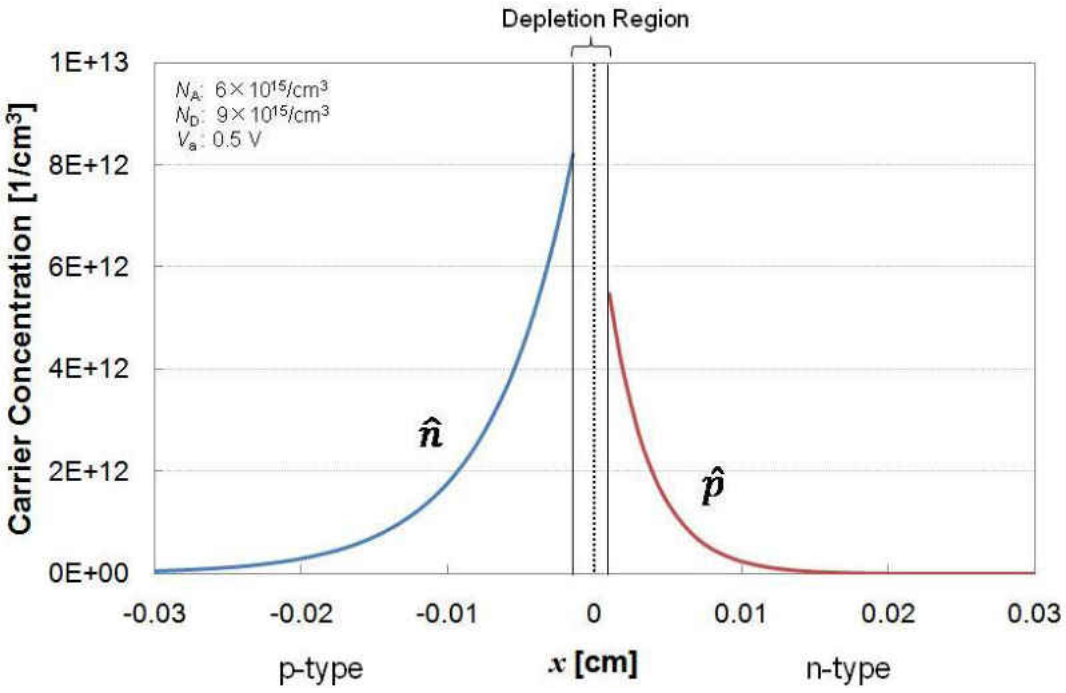

Figure 2-8: Distribution of excess minority carriers in forward bias condition

2.6.3 Photo-generated Current and Open Circuit Voltage

Current is the sum of the hole and electron flow at any point. The slope of the concentration curve of minority charge carrier determines the current contribution by each minority charge carrier. The hole current at the junction is given by [33]

$$I_{\mathrm{p}} = qA\sqrt{\frac{D_{\mathrm{p}}}{\tau_{\mathrm{p}}}\hat{p}_0} \qquad \cdots\cdots\cdots (2.28)$$

where A is the junction area. The electron current at the junction is given by [33]

$$I_{\mathrm{n}} = qA\sqrt{\frac{D_{\mathrm{n}}}{\tau_{\mathrm{n}}}\hat{n}_0} \qquad \cdots\cdots\cdots (2.29)$$

The total current is the sum of hole and electron currents as

$$I = I_{\mathrm{p}} + I_{\mathrm{n}} = qA\left(\sqrt{\frac{D_{\mathrm{p}}}{\tau_{\mathrm{p}}}\hat{p}_0} + \sqrt{\frac{D_{\mathrm{n}}}{\tau_{\mathrm{n}}}\hat{n}_0}\right) \qquad \cdots\cdots\cdots (2.30)$$

It is known that $n_{\mathrm{p}} = n_{\mathrm{p0}} + \hat{n}_0$ and also $p_{\mathrm{n}} = p_{\mathrm{n0}} + \hat{p}_0$

$$n_{\mathrm{p0}} = \frac{n_{\mathrm{i}}^2}{N_{\mathrm{A}}} \qquad \cdots\cdots\cdots (2.31)$$

$$p_{\mathrm{n0}} = \frac{n_{\mathrm{i}}^2}{N_{\mathrm{D}}} \qquad \cdots\cdots\cdots (2.32)$$

Therefore,

$$\hat{n}_0 = n_{\mathrm{p0}}\left[\exp\left(\frac{qV_\mathrm{a}}{kT}\right)-1\right] \approx \frac{n_\mathrm{i}^2}{N_\mathrm{A}}\left[\exp\left(\frac{qV_\mathrm{a}}{kT}\right)-1\right] \qquad \cdots\cdots\cdots (2.33)$$

$$\hat{p}_0 = p_{\mathrm{n0}}\left[\exp\left(\frac{qV_\mathrm{a}}{kT}\right)-1\right] \approx \frac{n_\mathrm{i}^2}{N_\mathrm{D}}\left[\exp\left(\frac{qV_\mathrm{a}}{kT}\right)-1\right] \qquad \cdots\cdots\cdots (2.34)$$

From equations (2.30) - (2.34), the total current, I can be written as

$$I = qAn_\mathrm{i}^2\left[\sqrt{\frac{D_\mathrm{p}}{\tau_\mathrm{p}N_\mathrm{D}}}+\sqrt{\frac{D_\mathrm{n}}{\tau_\mathrm{n}N_\mathrm{A}}}\right]\left[\exp\left(\frac{qV_\mathrm{a}}{kT}\right)-1\right] \qquad \cdots\cdots\cdots (2.35)$$

If the applied voltage is negative, reverse biased condition, reverse saturation current, I_0 is obtained as [33].

$$I_0 = -qAn_\mathrm{i}^2\left[\sqrt{\frac{D_\mathrm{p}}{\tau_\mathrm{p}N_\mathrm{D}}}+\sqrt{\frac{D_\mathrm{n}}{\tau_\mathrm{n}N_\mathrm{A}}}\right] \qquad \cdots\cdots\cdots (2.36)$$

From the relation between equation (2.35) and (2.36), current can be written as

$$I = I_0\left[\exp\left(\frac{qV_\mathrm{a}}{kT}\right)-1\right] \qquad \cdots\cdots\cdots (2.37)$$

Under illuminated conditions, an extra current is generated by photovoltaic effect. Therefore, the above equation reforms as [33]

$$I = I_0\left[\exp\left(\frac{qV_\mathrm{a}}{kT}\right)-1\right] - I_\mathrm{L} \qquad \cdots\cdots\cdots (2.38)$$

where I_L is photo-generated current as shown in Figure 2-9. When light is falling on a solar cell which is not connected to the external circuit, the generated free charge carriers are separated by

the built-in electric field until the system reaches equilibrium. Namely, when the built-in electric field is compensated by the stored charge carriers on both sides, equilibrium state is obtained. The corresponding potential is called open circuit voltage (V_{oc}) which is the maximum voltage a cell can provide. The open circuit voltage is given by [32]

$$V_{\mathrm{oc}} = \frac{kT}{q}\ln\left(\frac{I_{\mathrm{L}}}{I_0}+1\right) \approx \frac{kT}{q}\ln\frac{I_{\mathrm{L}}}{I_0} \qquad \cdots\cdots\cdots (2.39)$$

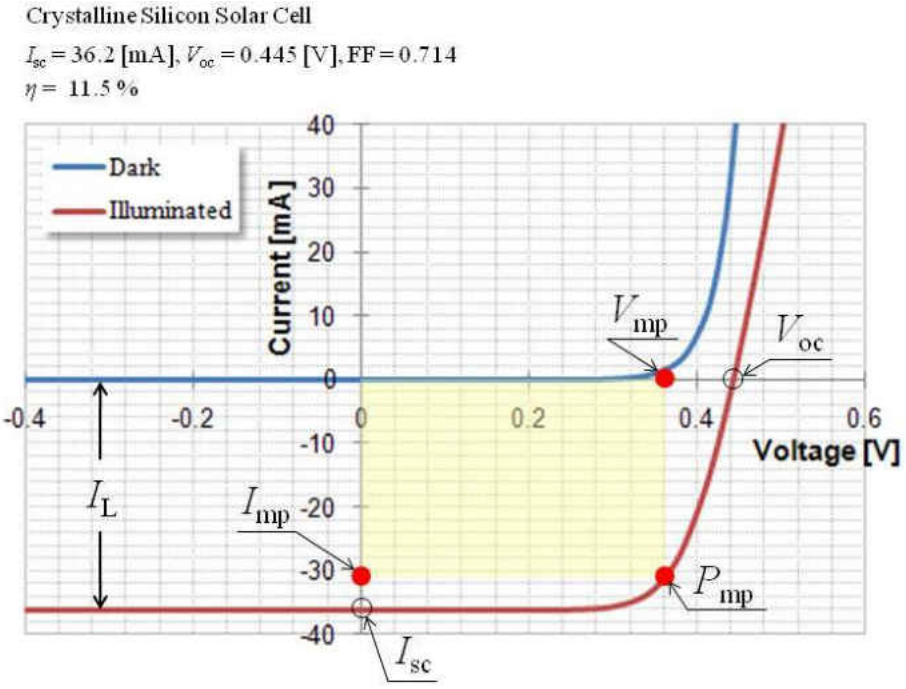

Figure 2-9: I-V characteristic of solar cell in dark and under illumination drawn in forth quadrant

2.6.4 Equivalent Circuit

Solar cells possess a series and shunt resistance in nature, as illustrated in the solar cell equivalent circuit of Figure 2-10. The I-V relationship of equivalent circuit is given by

$$\ln\left(I + \frac{I_{\mathrm{L}}}{I_0} - \frac{V - IR_{\mathrm{s}}}{I_0 R_{\mathrm{p}}} + 1\right) = \frac{q(V - IR_{\mathrm{s}})}{kT} \qquad \cdots\cdots\cdots (2.40)$$

Three parameters are usually used to characterize solar cell outputs. One of them is short circuit current, I_{sc}. Short circuit current is the current at short circuit condition, i.e. V=0. This I_{sc} is ideally equal to the photo-generated current, I_{L}. As a general practice, I_{sc} is represented as short circuit current density (J_{sc}) and it is the maximum current density a cell can produce. The second parameter is the open circuit voltage, V_{oc}. Ideal value of open circuit voltage is given by setting I to zero in equation (2.40). The maximum power is the optimum combination of voltage and current. The third parameter of fill factor (FF) is defined as the ratio of peak power to the product of V_{oc} and I_{sc}. It represents the "squareness" of the I-V curve, and given by [32]

$$\mathrm{FF} = \frac{V_{\mathrm{mp}} I_{\mathrm{mp}}}{V_{\mathrm{oc}} I_{\mathrm{sc}}} \qquad \cdots\cdots\cdots (2.41)$$

where V_{mp} and I_{mp} are respectively the voltage and current at the maximum power point, P_{mp} depicted in Figure 2-9. Highly efficient cells typically have a FF of greater than 70%. The photovoltaic conversion efficiency of a solar cell is given by the relation [32]

$$\eta = \frac{V_{\mathrm{oc}} J_{\mathrm{sc}} \mathrm{FF}}{P_{\mathrm{in}}} \qquad \cdots\cdots\cdots (2.42)$$

where P_{in} is the incident power taken as 1000 W/m^2 for a laboratory measurement corresponding to the AM 1.5 solar spectrum.

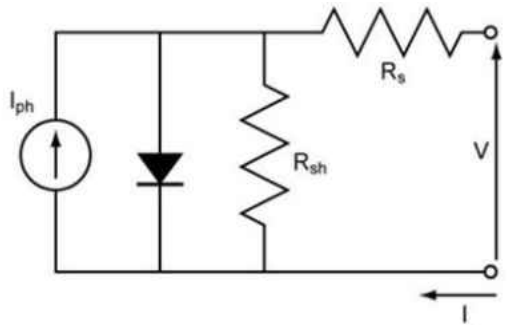

Figure 2-10: Equivalent circuit for solar cell

2.6.5 Device Parameters

The device parameters on the basis of which a cell's efficiency is defined are J_{sc}, V_{oc} and FF. These values depend on the kind of material and quality.

One of the factors which influence the value of J_{sc} is the light absorption ability, nominally referred to as absorption coefficient, α. The value of α depends on the type of band structure of the semiconductor. Direct band gap semiconductors such as CIGS can effectively absorb 90% of the light and produce electron-hole pair within 1 μm thickness (α=10^{-5}cm). Indirect band gap semiconductors such as silicon or germanium require additional energy to absorb photons. The additional energy to transfer an electron from the valence band to the conduction band is provided by phonon which is the form of lattice vibration. For example, α of

silicon is about 10^{-2} cm which requires approximately 100 μm thickness to effectively absorb 90% of the light.

Other important factors are drift and diffusion. When photons are absorbed within the built-in electric field, almost all electron-hole pairs can be separated by the electric field and contribute to the current. This field driven movement of the free carriers is called drift. Whereas, if photons are absorbed far away from the electric field, generated carriers do not lose their energy instantly and fall back into the bound state unless they encounter the built-in field. The amount of time for which they remain active is called lifetime. Within their lifetime, if the charge carriers do not get separated by the built-in field, they recombine and do not contribute to the current. The average distance a charge carrier can travel towards the built-in field within their lifetime is called diffusion length. The lifetime and diffusion length depend on the crystal quality of the material. Defects such as impurities, interstitials, lattice strain, vacancies and grain boundaries can work as recombination centers which reduce the diffusion length.

The V_{oc} depends on the built-in voltage of the device. Recombination centers located within the field results in continuous recombination of charge carriers and drastically reduce the V_{oc}. These recombination centers are called shunts. For a highly efficient cell, the current lost through shunts should be minimized, i.e. the shunt resistance, R_{p} should be high towards $+\infty$.

Another factor which causes the current and voltage loss is series resistance, R_{s}. Series resistances are the bulk resistances of semiconductor and metallic contacts, and the contact resistance between the metallic contacts and the semiconductor. Both R_{p} and R_{s} act to reduce the FF as indicated in Figure 2-11.

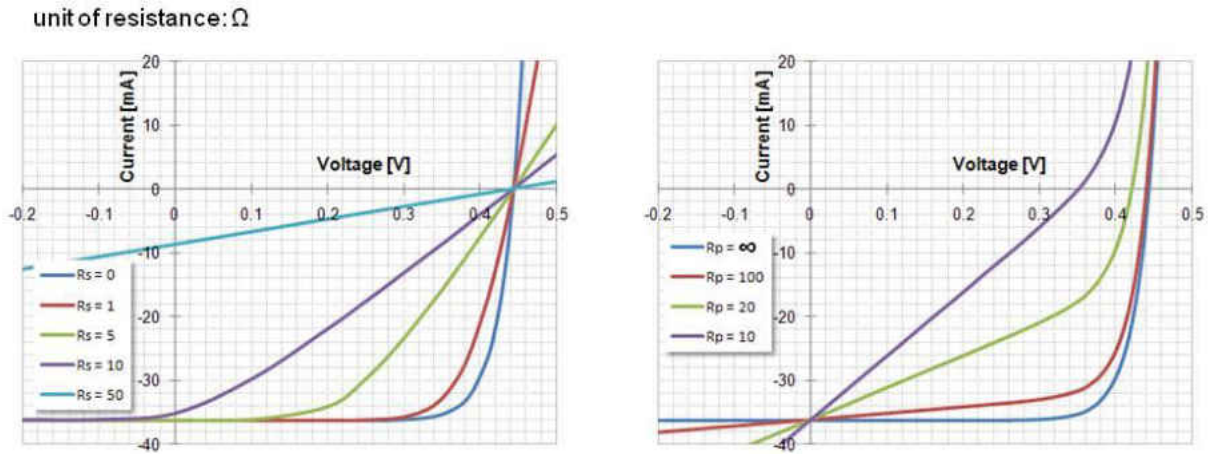

Figure 2-11: Effect of sheet resistance (R_s) and shunt resistance (R_p)

All the factors mentioned above can be measured by current-voltage and quantum efficiency (QE) measurements. QE measurement provides the information about the effectiveness of a cell in converting light into electricity. If a cell shows sensitiveness to high energy photons but poor response to low energy photons, it means the charge carriers generated within the built-in electric field effectively reach the metallic contacts, whereas those generated away from the field undergo recombination. This indicates that the diffusion length is considerably short due to the bad crystal quality. On the other hand, QE measurements showing poor response to high energy but good response to lower energy indicates the presence of a layer opaque to high energies and transparent to low energies or reflects high energy light preferentially. Such a layer could be removed or altered to improve the performance. The cells with a mediocre QE response indicate several problems. The obvious ones are the losses due to the reflection of the incident spectrum or large recombination losses at the junction that are removing a fraction of electrons independent of the energy of their original photons.

CHAPTER 3 MATERIALS REVIEW

Ever since the PV industry emerged on earth, crystalline silicon has dominated PV market as the major material for solar cells. Crystalline silicon is an indirect band gap semiconductor with a band gap of 1.12 eV. Being an indirect band gap semiconductor, silicon requires a minimum thickness of about 100 μm for the effective absorption of the solar spectrum.

During the early years of thin film solar cells evolution, considerable efforts were made for research, development and commercialization of Cu_2S/CdS cells. However, these efforts had to be abandoned as these cells had instability problems caused mainly by copper migration.

3.1 Cell Structure

A typical structure of CIGS solar cells is shown in Figure 3-1. Generally, following procedure is employed to fabricate a CIGS solar cell; however, note that the thickness of each layer is approximated number and can have a certain range of variation. First, a molybdenum (Mo) back contact layer with thickness of 1 μm is deposited onto a glass substrate using DC magnetron sputtering technique. Then 2 μm thick p-type CIGS light-absorbing layer is grown on top of the Mo layer at elevated temperatures ranging from 400°C to 600°C depending upon the employed process. Subsequently, n-type cadmium sulfate (CdS) buffer layer of 50 nm-thick is deposited by chemical bath deposition. An undoped ZnO (i:ZnO) layer is deposited, followed by a heavily aluminum doped ZnO (ZnO:Al) layer deposition, whose thicknesses are 50nm and

300nm respectively. This n-type ZnO bilayer is called window layer. Front contacts of aluminum-nickel (Al-Ni) alloy grid, for example, are formed on top of the window layer. Finally, Magnesium Fluoride (MgF_2) anti-reflection coating (ARC) is deposited over the finished device.

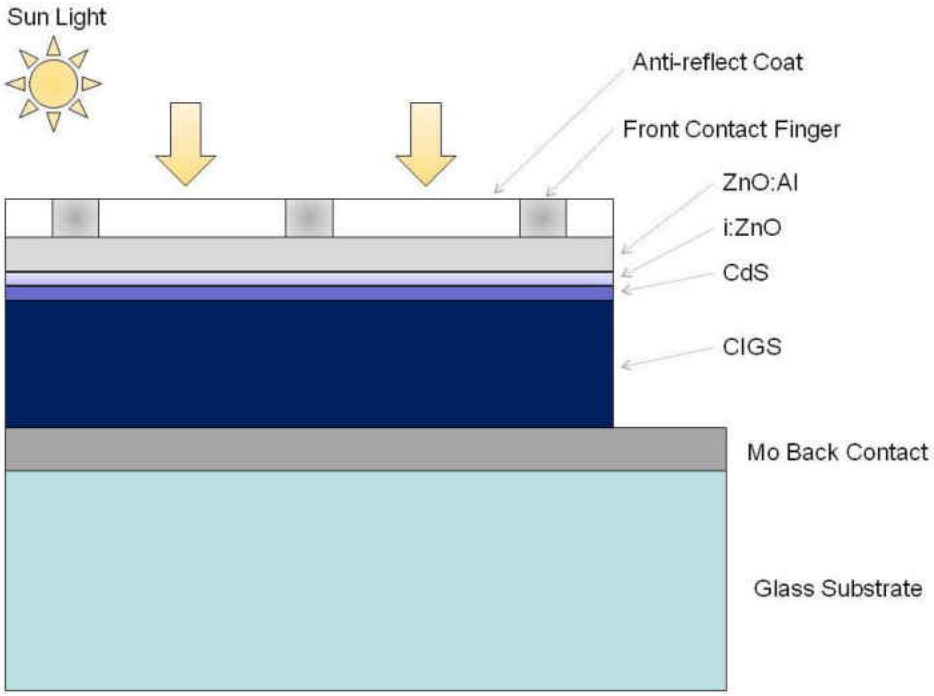

Figure 3-1: Cross sectional image of typical CIGS solar cell (not to scale)

3.2 CIGS Absorber

I-III-VI_2 compounds are proving to be promising materials as an absorber for solar cells to meet the increasing energy demand of the world. $CuInSe_2$ (CIS) and its alloys have shown long time stability; and highest energy conversion efficiency of 20% [9], [10] has been achieved

by NREL with CIGS/CdS system. CIS-based (hereinafter collectively called CIGS) solar cells are expected to supersede silicon solar cell because of their high efficiency as well as good possibilities of reducing energy generation cost and high throughput.

One of the excellent features of CIGS is its band gap adjustability. The band gap of CIS can be continuously widened by substituting Ga for In or S for Se. Namely, the band gap of CIS increases with the concentration of Ga or [35]. CIS has a direct band gap of 1.02±0.01 eV at room temperature with a temperature coefficient of $-2\pm1\times10^{-4}$ eV/K in the lower temperature regime [36]. The typical absorption coefficient is larger than 10^5/cm for 1.4 eV and higher photon energies [37]. Its excellent stability under high energy electron or proton flux has reported, which makes it an attractive material for aerospace applications [38], [39].

3.2.1 Material Fabrication

A wide variety of techniques are employed to fabricate CIS based absorber layer such as three-source evaporation [40], [41], laser ablation [42], [43], flash evaporation [44], [45], vapor transport [46], spray pyrolysis [47], [48], sputtering [49], liquid phase epitaxy [50], [51], electro deposition [52], [53], screen printing [54] and selenization of metallic layers [55], [56], [57]. Among the diverse ways of manufacturing CIGS thin-film absorbers, co-evaporation and two stage process techniques are the most promising in terms of cost reduction and energy conversion efficiency improvement.

3.2.1.1 Coevaporation Process

The highest energy conversion efficiency is obtained with CIGS based solar cell using thermal coevaporation from elemental sources. The process employs line-of-sight delivery of the Cu, In, Ga and Se sources. The film composition and growth rate depend on the flux distribution and effusion rate from the source. Initially, Boeing process was widely used [58] in which the film is deposited with Cu rich regime so that it forms a Cu_xSe phase, followed by In and Ga rich flux so that the composition becomes the desired Cu deficient. Later, the process has gone through several modifications, and a variety of ways are employed by variety of groups.

3.2.1.2 Two Stage Process

Sputtering technique is an established process for very high throughput manufacturing method. Two stage process is literally composed of two process stages. Namely, a base layer of precursor is prepared by sputtering technique, followed by annealing in selenium or sulfur atmosphere. ARCO Solar which later became Shell Solar is the pioneering manufacturer of CIS solar cell fabrication using the two stage process [59].

The two stage process developed by ARCO Solar employs sputtering of a Cu and In layer on Mo-coated glass substrate as the first step. In the second step, the Cu-In precursor is exposed to a selenium-bearing gas such as hydrogen selenide (H_2Se) mixed with argon at the elevated temperature. The H_2Se breaks down and leaves selenium atom when it reaches on the precursor surface, then the adsorbed Se chemically reacts with Cu and In so that the precursor transforms into a very high quality CIS absorber. Sputtering technology has the great advantage of expandability in scale and adaptability to roll-to-roll production on flexible substrates.

3.2.2 Crystal Structure

I-III-VI_2 semiconductor material family crystallizes in tetragonal chalcopyrite lattice structure and is stable from room temperature up to 810°C [60]. Chalcopyrite has a diamond-like structure similar to zinc sulfide (ZnS) structure in which Zn atoms are replaced alternatively by Cu (I) and In (III) atoms giving it a tetragonal unit cell. Each Cu and In atom has four bonds with Se (VI) atom. In an opposite manner, each Se atom has two bonds to Cu and two to In described in Figure 3-2. Since bond strength of the I-VI and III-VI bonds is generally different, the tetragonal lattice parameters, c/a is not exactly 2. The deviation from $c/a = 2$ is called the tetragonal distortion which is -0.01 in $CuInSe_2$ and +0.04 in $CuGaSe_2$.

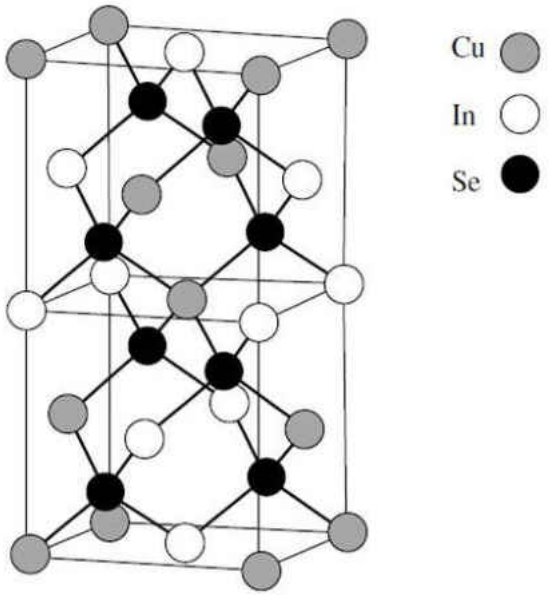

Figure 3-2: $CuInSe_2$ chalcopyrite crystal structure [34]

3.2.3 Band Gap

The band gap energies of I-III-VI_2 are considerably smaller than those of their binary analogues because the Cu 3d band, together with the Se 4p band, forms the uppermost valence band in the Cu-chalcopyrite, which is not so in II-VI compounds. However, the system of Cu-chalcopyrite covers a wide band gap of energies from 1.02 eV in $CuInSe_2$ up to 2.4 eV in $CuGaSe_2$, covering most of the visible spectrum.

3.2.4 Phase Diagram

The phase diagram provides the alloy composition, the allowed deviation from the stoichiometry and the process temperature for producing a high-quality absorber layer. Figure 3-3 shows the ternary elemental composition diagram of Cu-In-Se system. Thin films in this system grown with excess supply of Se have compositions that lie on, or near, the tie line between Cu_2Se and In_2Se_3. Note that the ordered defect compounds (ODC) such as $CuIn_3Se_5$, $Cu_2In_4Se_7$ and $Cu_3In_5Se_9$ lie on the same tie-line as well as $CuInSe_2$ and have the same chalcopyrite structure. Because the ODC are formed by ordered arrangements of intrinsic point defects, they maintain the chalcopyrite crystal structure [34]. This complex ternary diagram can be reduced to a simpler pseudo-binary phase diagram near $CuInSe_2$ along the tie-line and is shown in Figure 3-4 [61].

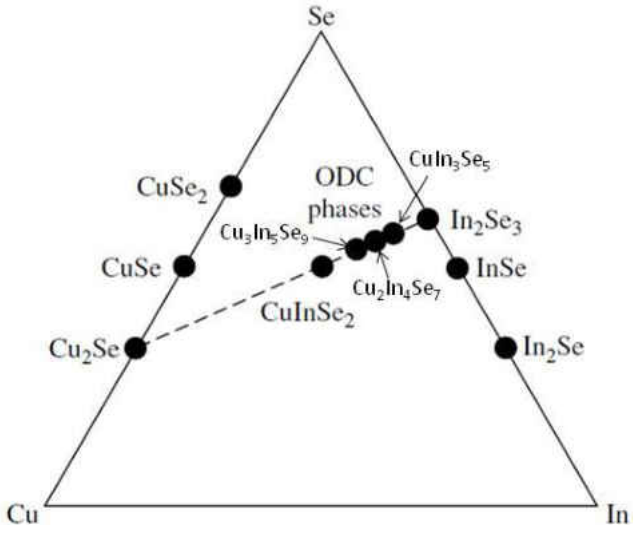

Figure 3-3: Elemental composition diagram of Cu-In-Se ternary system [34]

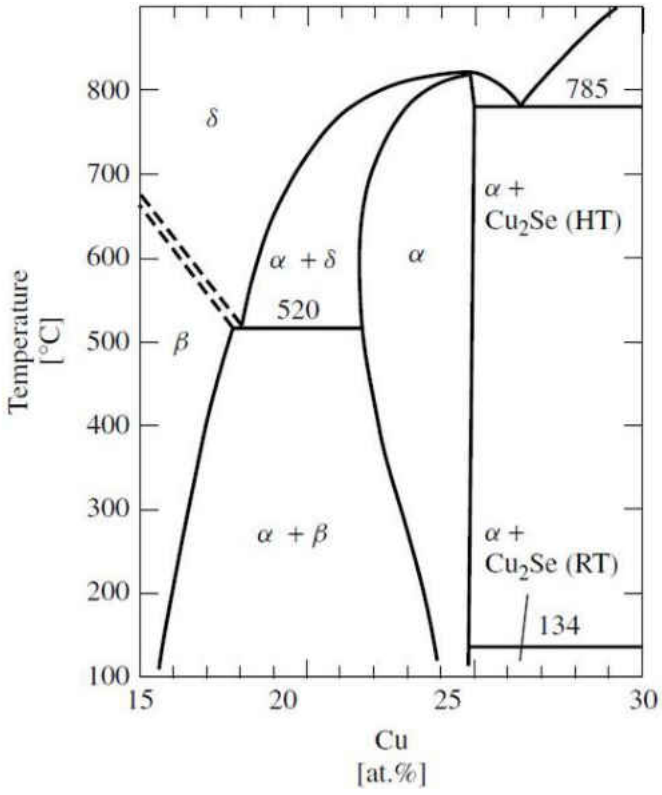

Figure 3-4: Pseudo-binary phase diagram along the tie line between Cu_2Se and In_2Se_3 [34]

3.2.4.1 α-Phase

According to the phase diagram, the α-phase ($CuInSe_2$) can exist in a relatively narrow range of Cu composition from 24 to 24.5 at% at room temperature, whereas at higher temperature between 500°C and 550°C, the α-phase exists in the range of 22 to 24.5 at% Cu. However, it has been reported that a certain amount of addition of either gallium or sodium widens the α-phase region at room temperature to the range of 22 to 24.5 at% Cu. It is also noted that the composition rate is not stoichiometric and Cu composition is less than 25 at%.

3.2.4.2 β-Phase

Because CIS thin films are grown at high temperatures, the α-phase region widens toward the In rich side, there is quite a high possibility that the cooled film contains β-phase ($CuIn_3Se_5$). Some groups have reported the benefits of having such an ODC layer built by ordered arrays of defect pairs of Cu vacancies and In on Cu antisites [62]. This ODC layer has a wider band gap of 1.3 eV than that of CIS. By employing a wider band gap semiconductor at the metallurgical junction, V_{oc} increases [63].

3.2.4.3 Cu_2Se phase

When the absorber layer is grown in Cu-rich regime an additional Cu_2Se phase is formed on the CIS grain boundaries. This additional layer is metallic in nature, therefore, it has to be removed before depositing the heterojunction partner.

3.2.4.4 δ-Phase

Another phase that appears in the phase diagram is the δ-phase with the sphalerite structure which is stable at high temperature. A congruent solid-solid phase transformation occurs at 810°C between the disordered δ-phase and the ordered chalcopyrite α-phase.

3.2.5 Intrinsic Defect Doping of CIGS

3.2.5.1 Defects

Another important characteristic of CIS based materials is that they can accommodate a large amount of compositional variation without causing substantial changes in the electronic properties. As a matter of fact, highly efficient solar cells have been fabricated with Cu/(In+Ga) ratio between 0.7 and 1. This excellent property can be explained on the basis of defect chemistry of CIS.

It has been shown that the formation energies of copper vacancies V_{Cu} and defect complex composed of two copper vacancies in combination with In antisite on Cu ($2V_{Cu}+In_{Cu}$) are low [64]. V_{Cu} introduces a shallow acceptor that is responsible for the p-type conductivity of CIGS. Isolated In_{Cu} acts as a deep donor level; however, it can be electrically neutralized when combined with $2V_{Cu}$, thus, the $2V_{Cu}+In_{Cu}$ defects prevent degenerate doping in In rich material. Because of the high concentration of $2V_{Cu}+In_{Cu}$ complexes, they interact with each other and reduce the formation energy further.

Thus the formation of such defect complexes can compensate the off stoichiometry of CIS based material in Cu-poor or In-rich composition without introducing unfavorable effects on electrical properties.

3.2.5.2 Doping

Electric properties of the CIS based semiconductors are controlled by intrinsic defects. If a CIS semiconductor is grown in Cu poor and Se rich condition, it shows p-type conductivity, whereas Cu-rich material grown with Se deficient condition tends to show n-type characteristic [65], [66]. Thus, Se vacancy (V_{Se}) is considered as the dominant donor responsible for the n-type characteristic as well as acts as a compensating donor in p-type CIS based material, whereas V_{Cu} is dominant acceptor in Cu poor p-type material.

If there is excess Cu, major defects are Cu_{In} antisite and In vacancy (V_{In}) acceptors, which both contribute to a formation of a p-type characteristic.

3.2.5.3 Grain Boundaries

A variety of defects such as dislocations, stacking faults and twins have been reported on grain boundaries of CIS based materials [67], [68], [69]. One of the most harmful defects on grain boundaries and surface is selenium vacancy, V_{Se}. However, V_{Se} can be passivated with oxygen and electrically harmless by heat treatments in air atmosphere without affecting the bulk chemistry. As a result, grain boundaries become more p-type due to the elimination of deep donor level and become electronically benign.

3.2.6 Band Gap Engineering

3.2.6.1 Gallium Incorporation

CIS has a direct band gap of 1.02 eV at room temperature; however, it is narrower than the ideal value for solar cells. It has been suggested that incorporating Ga will widen the band gap and make it closer to the ideal value. Incorporation of Ga results in an increase of the band gap of CIS by increasing the conduction band minima [64]. The increase in band gap with gallium content rate, x is estimated by [70]

$$E_g[\text{eV}] = 1.010 + 0.626x - 0.167x(1-x) \qquad \cdots\cdots\cdots (3.1)$$

Gallium has a tendency to diffuse towards the back metallic contact because of its small size and residual stress in the film [71]. As a consequence, CGS phase (copper gallium diselenide) is formed in the high Ga content region near the back contact [72]. CGS has a band gap of 1.68 eV which is wider than CIS. Hence, the band gap gradient is created between CIS surface region and CGS back contact region which act as a back surface field (BSF) that repels minority carriers diffusing into the back contact. The BSF greatly reduces the charge carrier loss at the back contact and increases the open circuit voltage [73].

Another beneficial effect is obtained from the fact that the formation energy of a Ga_{Cu} defect is higher than the formation energy of In_{Cu}. This higher energy discourages the formation of defect pairs of $2V_{Cu}+In_{Cu}$, thereby reducing the tendency to form the ODC [74] and enhancing the α-phase formation.

3.2.6.2 Sulfur Incorporation

Sulfurization of metallic precursors in a sulfur atmosphere is another technique to expand the band gap of CIS or CIGS up to 1.55 eV. Hahn-Meitner-Institut of Germany has developed a similar process using elemental sulfur [75]. Post sulfurization treatment yields CIGSS or CIGS2 layer at the surface area. Forming a wider band gap at the p-n junctions helps the device increase the V_{oc}. During post sulfurization treatment, sulfur atoms tend to occupy selenium vacancies or replace selenium in crystal because sulfur is more reactive compared to selenium, thereby it reduces the compensating donors, $V_{Se,}$ and passivate the surface as well [76].

3.2.7 Effect of Sodium Addition

The highly efficient CIGS thin-film solar cells have been employing soda lime glass as a substrate material which contains considerable amount of sodium (Na) in the form of Na_2O. It has been shown that the incorporation of certain amount of Na during growth of the CIGS layer is favorable for the solar cell performance reducing detrimental point defects.

Na reduces compensating donors by occupying selenium vacancies and In_{Cu} antisite defects, thereby increase the p-type conductivity [77]. Moreover, Na also replaces copper vacancies to reduce the formation of ODC and increase the α-phase area in the phase diagram. It is reported that the grain size is enlarged by promoting preferred grain growth orientation (112) [78] and Na on the grain surfaces and boundaries acts as a catalyst for the oxygen passivation [79].

3.3 Window Layer – Cadmium Sulfate (CdS)

Cadmium sulfate (CdS) semiconductor has been widely and deeply investigated and a variety of techniques have been applied to fabricate solar cell quality layers. [80]. CdS is a n-type semiconductor with a band gap of 2.45 eV and forms a heterojunction with CIS based absorbers. Most part of the depletion region at the interface is in the CIS film because the carrier density in CdS is much larger than CIGS, which results in reduction in the minority carrier recombination at the back metallurgical contact. It is also known that CdS can grow epitaxially on CIS surface [81]. Due to its wide band gap and transparency, CdS serves as a window layer with small light absorption.

A 50 nm thick film shows yellow to orange color but when it is grown on a CIGS film, it looks blue to purple. The optical absorption edge of CdS films grown with CBD is the same as that of bulk material.

CdS films are usually grown by chemical bath deposition (CBD), and the crystal structure can be varied depending on the deposition parameters [82]. CdS thin film deposited by CBD has wurtzite crystal structure where the c axis is perpendicular to the substrate. The growth orientation is in a closed packed direction <0001>.

Chemical bath deposition of CdS buffer layers on CIGS absorber is generally carried out in an alkaline aqueous solution of pH>9, which contains cadmium salt ($CdSO_4$), complexing agent (NH_3) and sulfur precursor ($(NH_2)_2CS$, Thiourea). The complexing agent plays a role of decelerating the reaction and avoids the formation of $Cd(OH)_2$. The temperature range of 60 to

80°C is generally employed for thiourea to hydrolyze, decompose, and then release S^{2-} ions. The net reaction for the formation of CdS is as follows:

$$Cd(NH_3)_4^{2+} + SC(NH_2)_2 + 2OH^- \rightarrow CdS + H_2NCN + 4NH_3 + 2H_2O \qquad \cdots\cdots (3.2)$$

There are quite a few benefits obtained by a CdS layer deposition:

1. CBD deposition of CdS evenly covers the rough CIS polycrystalline absorber surface.
2. The CdS layer protects against damages and chemical reactions from subsequent ZnO deposition process.
3. The chemical bath solution removes the natural oxide layer on the film surface and re-establishes positively charged surface states. As a consequence, there is a natural type inversion at the buffer/absorber interfaces.
4. Cd diffuses into the Cu-poor CIS surface layer at tertian depth and forms Cd_{Cu} donor, thereby it provides additional positive charge that enhances the type inversion of the buffer (CdS)/absorber interface [83].
5. From the electrical point of view, CdS layer optimizes the band alignment of the device [84] and forms a wide depletion region that minimizes tunneling and establishes a higher contact potential that allows higher open circuit voltage [85].

3.4 Window Layer – Zinc Oxide (ZnO)

3.4.1 i:ZnO Buffer Layer

Highly resistive undoped ZnO (i:ZnO) is commonly used as a buffer layer between CdS and top transparent conductive layer. Due to its intrinsic defects which act as shallow donors such as oxygen vacancies (V_O) and zinc interstitials (Zn_I), i:ZnO has n-type conductivity [86], [87]. Typically thickness of 50 nm i:ZnO layer is deposited by radio frequency (RF) magnetron sputtering technique. The highly resistive layer prevents the direct contact of transparent and conducting oxide (ZnO:Al) layer and CIGSS absorber or even Mo back contact, thereby eliminates the shunt paths. The thickness of i:ZnO layer is very critical to the device performance. If the layer is too thin, it may allow the leakage current to increase. On the other hand, an excessively thick layer increases the series resistance, which reduces the current density. The i:ZnO layer also significantly influences the V_{oc} and the FF [88].

3.4.2 Transparent Conducting ZnO Layer

ZnO is a low-cost and abundant material with a band gap of 3.3 eV making it transparent to the visible spectra. A Group III element such as aluminum, boron or gallium is doped to achieve a high conductivity. Among all the variety, aluminum doped ZnO:Al is frequently used as a transparent and conducting front contact in thin-film solar cells with CIGS absorber. RF or DC magnetron sputtering technique is used to deposit the layer. The target material usually contains 2 wt% of alumina (Al_2O_3) for high conductivity. It has hexagonal wurtzite lattice

structure and shows n-type conductivity because of the non-stoichiometry. Highly dense charge carrier makes ZnO:Al low resistive transparent conducting layer.

Introduction of electrically active defects into ZnO layers deposited by sputtering strongly depends on process parameters such as working gas pressure and flux, RF power and the distance between the target and the substrate. Growing in oxygen deficient condition leads to the deposition of opaque metallic zinc along with zinc oxide. Therefore, oxygen gas is incorporated to the sputter gas to grow transparent layer, or the substrate is heated to re-evaporate free zinc atoms.

3.5 Molybdenum Back Contact Layer

Molybdenum (Mo) is one of the most important materials used as a back Ohmic contact layer for CIS based thin-film solar cells. A variety of metal/CIS contacts have been investigated, including Mo, Pt, Au, Au/Be, Al, Ni, Ag, and Cu. These studies have shown that Pt, Ni, Au, and Mo all form fairly reproducible, low-resistance contacts to CIS. However, if they are annealed at elevated temperatures Au and Pt swiftly diffuse into the CIS layer [89], whereas Mo and Ni seem to be inert and can be even improved with high-temperature treatment [16]. The contact properties of CIS films formed at high temperatures (600°C and above) on metallic thin films are likely to be quite different [90]. Moreover, for polycrystalline CIGS solar cells, the metallic back contact is the substrate where the CIGS absorber layer grows. Because of its relative stability at the processing temperatures, chemical stability against reacting with Cu, In and Ga, and its low

contact resistance to CIS based material, Mo has been dominantly selected for the back contact layer to CIS and CIGS solar cells [91].

3.5.1 Residual Stress and Resistivity

Mo back contact is generally deposited by DC magnetron sputtering; however, it develops residual stress during the deposition process. It has been reported that the internal stresses in refractory-metal films prepared by magnetron sputter deposition are strongly influenced by the working gas pressure [20], [92]. Being a refractory-metal, Mo shows a correlation between working gas pressure and residual stress when deposited by DC magnetron sputtering deposition technique [30], [11], [29].

Macroscopic stresses may be observed by visual assessment. If films are in a highly compressive stress state, they tend to buckle up, whereas films under substantial tensile stress show scratch patterns [11], [93].

It is suggested that such residual stress developments are dependent on energetic flux of reflected neutral atoms and/or sputtered atoms from the target. The working gas molecules play a critical role of reducing the flux and energy of these atoms. At lower pressures, the mean free path of the energetic particles become longer, thereby the bombarding atoms have higher kinetic energy. As a consequence, the deposited film has a densely packed microstructure which is responsible for the tendency towards the compressive stress state. In other words, one can say that this compressive stress is introduced by atomic peening effect of energetic particles. Whereas, at higher pressures, the mean free path becomes shorter and particles have higher

probability to be scattered, thereby less energetic particle incidence is served to the film. The resulting film tends to exhibit an open porous microstructure. Due to its open structure, interatomic or intergranular attractive forces become high, hence produces tensile stress.

Likewise, open structure increases the resistivity of Mo thin films. Therefore, resistivity is strongly dependent on working gas pressure condition. High pressure condition yields low resistive, and low pressure condition yields high resistive Mo thin films.

3.5.2 Surface Roughness and Morphology

It has been reported that surface roughness of substrate may influence the device performance as a CIGS solar cell through following three mechanisms [94].

1. *Nucleation*. A rough Mo coated substrate surface is supposed to provide more sites to nucleate for CIGS absorber, resulting in smaller CIGS grains and more defects.
2. *Impurity diffusion*. A number of impurities diffuse from the soda lime glass substrate into the CIGS layer through the Mo back contact during the growth process of the CIGS absorber layer at elevated temperature. As mentioned in earlier section, Na is known as a fast diffuser and a beneficial impurity for CIGS solar cells; however, the amount of incorporation has to be controlled for repetitive stable CIGS solar cell production. Defects and grain boundaries in Mo layers provide fast diffusion paths for all impurities. Therefore, it is important to control the impurity diffusion by controlling the microstructure of Mo back contact layers.

3. *Metallurgical shunts*. Large surface projections of Mo back contact layer may protrude through CIGS absorber layer to create shunt paths.

CHAPTER 4 EXPERIMENTAL SETUP

To find out how sputtering deposition parameters such as working gas pressure and DC power supplied to the sputtering system influence the properties of Mo thin films, following equipments, experimental procedure, and measurements were employed in this work.

4.1 Sputtering System

Mo thin film deposition was carried out by DC magnetron sputtering technique. The vacuum chamber was evacuated to the base pressure of 1.5 to 2.0 $\times 10^{-6}$ Torr using a combination of a mechanical pump and a cryo pump [55]. During the sputtering process, only the cryo pump was operated to set a pressure at the desired value. A schematic diagram of the employed sputtering system to deposit the Mo thin films is shown in Figure 4-1. The distance between the planar magnetron sputtering cathode target and the substrate was maintained at 90 mm for all depositions. The substrate can slide linearly over the target using a computer controlled stepper motor.

Depositions were carried out from the Mo cathode target dimensions of 300 × 100 mm and purity of 99.95%. The Mo cathode target was water-cooled during the deposition process to avoid the target get damaged. The Mo target was fabricated from commercially available material. The soda lime glass substrate was placed on the stainless steel holder and loaded into the deposition vacuum chamber. A 99.999% pure argon (Ar) gas was used as a working gas and

its flow rate was varied with a mass flow controller to set the desired gas pressure. Ar pressure was measured with a convectron gauge.

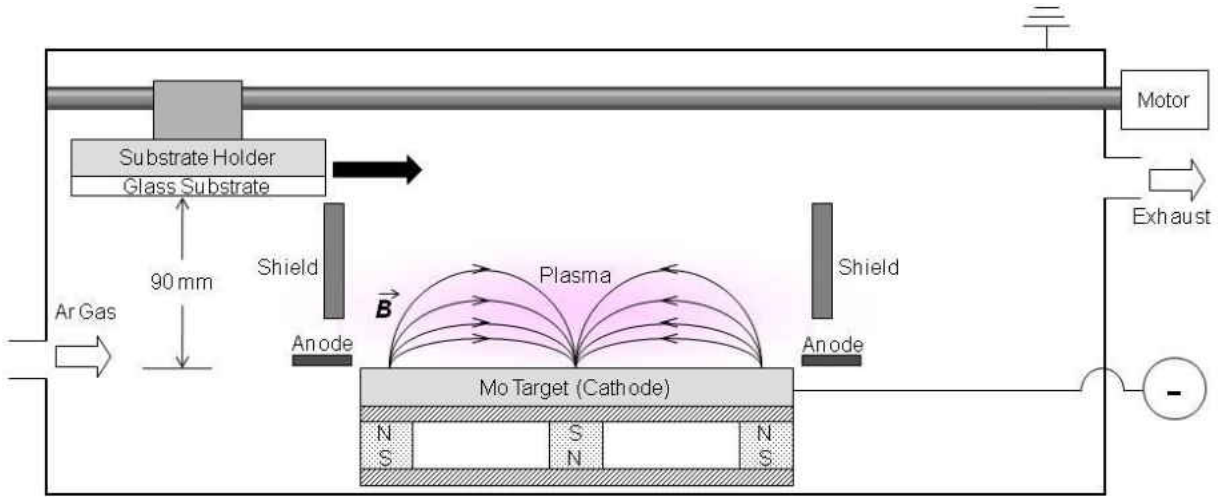

Figure 4-1: DC magnetron sputtering system

4.2 Process Procedure

4.2.1 Substrate Preparation

Prior to the deposition, the glass substrate was cleaned by detergent solution, ultrasonic, and deionized water. After scrubbing with detergent solution, and ultrasonic cleaning, the substrate was rinsed in running deionized water. After the rinse, the substrate was blow-dried with high purity nitrogen gas, then immediately introduced into the vacuum chamber to avoid attachment of contaminations and particles to the substrate. The thin flat glass strips used for the bending beam measurement were cleaned by wiping with deionized water and isopropanol.

Properties such as resistivity, surface roughness, crystallinity, and thickness were measured with the Mo thin films deposited on the 3 mm thick soda lime glass substrate. Residual stress of Mo thin films was measured by the deflection of the very thin glass strips after the Mo film deposition.

4.2.2 Process Plasma

The following procedure was used for lighting the process plasma.

1. The chamber was evacuated to a base pressure below 2.0×10^{-6} Torr.

2. The gate valve was throttled to maintain the pressure of the chamber during deposition.

3. Introduce Ar gas into the chamber to raise the chamber pressure up to a desired value to be maintained during the sputtering process.

4. The DC power supply was turned on with initial power supply of 50W, and the power was gradually increased by the controller until the power reaches a desired value.

The planar magnetron cathode was operated in the power control mode, and horizontal shields provided a symmetric coating window with a maximum incident angle of approximately 40°. Preparatory for the deposition, the target surface was cleaned by "pre-sputtering" which is typically 5 minutes operation under the deposition conditions to be employed, while the substrate was isolated from the plasma by the shields.

4.2.3 Deposition

During the deposition process, the substrate was slowly transported over the target using a stepper motor. The transportation time was determined from the deposition rate and the desired thickness of the Mo thin film, and the motion speed of the substrate was controlled by a computer program. The purpose of the transportation of the substrate is to eliminate the position dependency of the properties and thickness within the film. By moving the substrate horizontally above the target, the incidence angle of the target atom flux varies with position; eventually all portion of the substrate are equally exposed to the varied flux, and a homogeneous film deposition on the substrate is achieved. Under these process conditions, a variation in Mo film thickness of less than 5% was obtained.

4.2.4 Substrate Temperature

During the deposition of Mo film, the glass substrates were not given any thermal control. The temperature increase of the substrates during sputter deposition was estimated to be less than 50K, corresponding to a negligible thermal stress condition of approximately 0.05 GPa. Therefore, the deflections due to thermal effects during deposition are negligibly small compared to the deflection caused by film stress [28].

4.3 Measurements

All measurements on films were made after the samples had been unloaded from the sputtering system. All data were measured immediately after the unloading to avoid aging except for XRD and AFM measurement, which were measured at NREL and University of South Florida.

4.3.1 Stress Analysis

The residual stress was measured by the bending beam method. Experiments were carried out on a 0.15 mm thick, dimension of 10mm × 150mm rectangular soda lime glass strip to obtain qualitative information about the stress developed under various parameters of deposition. Thin flat glass strip was attached to a 3 mm thick, dimension of 6 × 4 inch glass substrate along the 300 mm length of the target gluing them with vacuum compatible tape only at the two ends [95].

Mo films were deposited onto the running glass substrates at Ar pressure ranging from 0.1 to 5.0 mTorr and supplied power ranging from 200 to 300 W. Target voltages and plasma currents were varied dependent on both working gas pressure and supplied power conditions.

Measured deflection displayed by the glass strips were along the 300 mm length of the Mo target. The nature of the bending in the glass strip was either convex or concave depending on the stress state. The bending of the film/strip assembly is caused by the presence of internal stresses: stresses are compressive in the film when the convex side of the assembly is the film. Any change in the internal stress state will result in a change in the radius of curvature. Extensive

studies have examined and modeled this phenomenon, as reviewed by Benabdi and Roche [96]. Most of these works follow the one-dimensional analysis of Stoney [97], who derived the classic expression relating the radius of curvature of the deposited thin film, R to its internal residual stress, σ_{i} in case where the films are much thinner than the substrates [98].

$$\sigma_{\mathrm{i}} = \frac{E_{\mathrm{s}} h_{\mathrm{s}}^2}{6(1-\nu)h_{\mathrm{c}}}\left(\frac{1}{R} - \frac{1}{R_0}\right) \qquad \cdots\cdots\cdots (4.1)$$

where E_{s} is the Young's modulus of the glass strip, h_{s} is the thickness of the strip, h_{c} is the film thickness, ν is the Poisson's ratio of the strip, R and R_0 are the radii of curvature of the strip after and before deposition, respectively. Division by (1-ν) is to take into account that the stress in the film is biaxial. Stoney's equation can be reformulated to give

$$S = \left[\frac{4E_{\mathrm{s}}{h_{\mathrm{s}}}^2}{3(1-\nu){L_0}^2}\right] \times \left[\frac{\delta}{h_{\mathrm{c}}}\right] \qquad \cdots\cdots\cdots (4.2)$$

where S is the average stress of the film, L_0 is the length of the glass strip, δ is the deflection at the end of the strip depicted in Figure 4-2. Here, the term of the original curvature of a bare glass strip, $1/R_0$ is set at naught because it is much larger than that of after depositon. Relationship among R, δ, and L_0 is geometrically given by

$$R = \frac{{L_0}^2}{8\delta} \qquad \cdots\cdots\cdots (4.3)$$

The usual convention, where compressive stresses are negative, was adopted. Timoshenko [99] initially proposed to correct for higher orders of the thickness ratio, $h_{\mathrm{c}}/h_{\mathrm{s}}$, and refined corrections to Stoney's equation, according for different values of Poisson's ratio and different

substrate thickness and substrate width have since been derived. Such corrections turn out to be less than a few percent if the radius of curvature, R is greater than, or approximately equal to W^2/h_s, where W represents substrate width [100]. Stoney's equation was corrected by Hofmann for the case of biaxial in-plane stress [101]. Alternative expressions delivered in the past decades are numerous, a critical assessment of which can be found in elsewhere [96], [102].

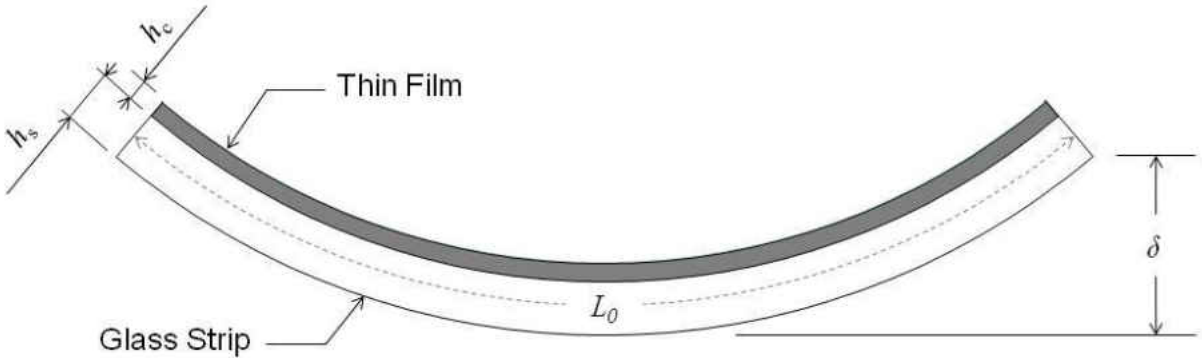

Figure 4-2: Schematic of bent glass strip and thin film

4.3.2 Crystallinity

Crystal structure was investigated using X-ray diffraction (XRD) technique with Cu Kα radiation (wavelength = 1.540562 Å). From the obtained XRD spectral patterns, lattice parameter and mean grain size for each film deposited with different condition were estimated.

4.3.3 Resistivity

From an electrical point of view, sheet resistance should be as low as possible for a back contact layer of a solar cell to minimize the influence to the series resistance of the cell. Sheet resistance of Mo thin films was measured using a four-point probe measurement technique. Sheet resistances varied by no more than 5% across the 6×4 inch substrate area. Then, resistivity of the Mo thin films was calculated from the sheet resistance and thickness of the film.

4.3.4 Thickness and Roughness

Dektak profilometer was used to determine the Mo film thickness and surface topography. Thickness was measured at a step between bare glass and deposited film, which had been created by attaching the mask during the deposition process. Among a number of parameters and functions which are employed to describe the surface features, average roughness (R_a) was used to describe the feature of the Mo film surface. R_a is defined as the arithmetic mean of the departures of the profile from the mean line. The scan length of 2 mm for the average roughness measurement was arbitrarily selected. The low pass filter of 200 μm was used to remove waviness components from the R_a calculation because the waviness is considered to originate from the soda lime glass substrate and not to be effective to the CIGS solar cell performance. Atomic force microscopy (AFM) was also used to cover more detail resolution.

4.3.5 Adhesion

The degree of adhesion was qualitatively assessed using the "Scotch-tape" test [100]. Adhesion is considered to be adequate if the Mo thin film is not pulled off by the tape when it is removed promptly.

CHAPTER 5 RESULTS AND DISCUSSIONS

5.1 Plasma Discharge Characteristics

The practical relationship between plasma discharge current, I and discharge voltage, V in a magnetron sputtering system can be empirically given by [103]

$$I = \kappa V^n \qquad \cdots\cdots\cdots (5.1)$$

where both κ and n are constants. These constants are strongly dependent on the gas-target combination, the design of the magnetron system, the magnetic field, and other geometric parameters. The value of n is generally in the range of 5 to 15 [103].

Figure 5-1 shows the obtained I-V characteristics of the sputtering system, and Table 5-1 shows the process conditions employed in this investigation. The n values for pressures of 0.1, 0.3, and 1.0 mTorr are 3.20, 3.56, and 6.22, respectively. The lower value of n obtained at lower pressure indicates the target-gas combination has lower yield [104]. The increase of the n value at higher gas pressure indicates that the yield is improved by increasing the pressure. Namely, the increase of the gas pressure causes the reduction of the electron temperature (T_e), which stems from the collision frequency difference. The electron temperature reduction brings the voltage drop given by,

$$V = \alpha (kT_e)^{0.5} \qquad \cdots\cdots\cdots (5.2)$$

where α is a constant for the sputtering system. The n value increases to compensate the voltage drop at higher working gas pressure condition. In other words, the sputtering power dents to be

used to increase the plasma current at higher pressure. Hence, the pressure should be low to achieve a higher discharge voltage.

Table 5-1: Process conditions for discharge current and voltage characteristics

Pressure [m Torr]	Power [W]	Voltage [V]	Current [A]
0.1	200	289	0.691
	225	296	0.759
	250	306	0.818
0.3	200	293	0.683
	225	301	0.748
	250	308	0.813
1.0	200	295	0.678
	225	299	0.753
	250	304	0.822

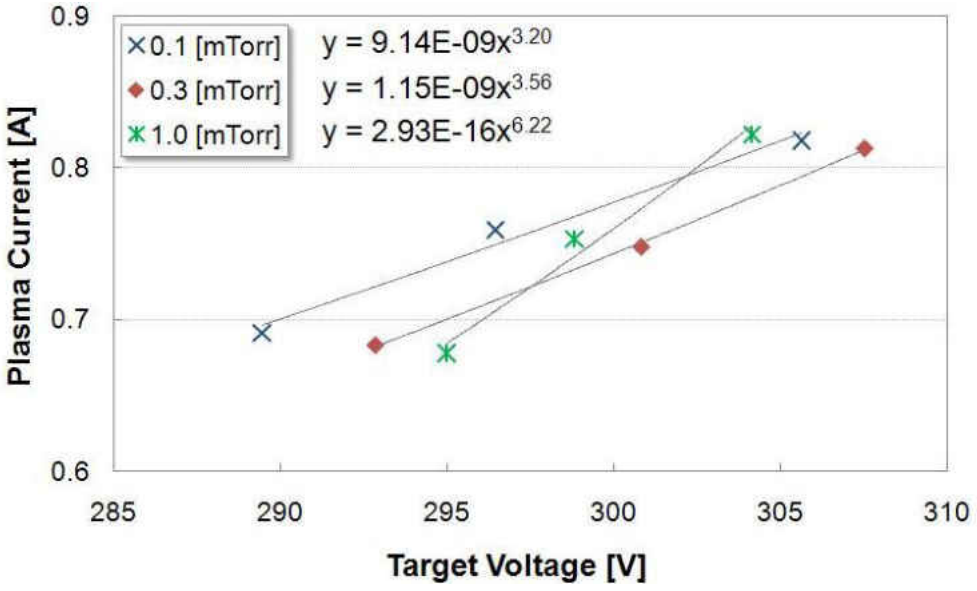

Figure 5-1: Relationship between discharge current and voltage of the sputtering system at pressures of 0.1, 0.3, and 1.0 mTorr

5.2 Deposition Rate

The deposition rate and uniformity are commonly scaled with the product value of the working gas pressure and the working distance between target and substrate. However, this scaling is complicated by the flux of the neutralized backscattering gas atom. The deposition rate is shown if Figure 5-2 as a function of sputtering power. By varying the sputtering power and the working gas pressure, the deposition rate varied from 3.3 to 5.6 Å/s.

The deposition rates showed the strong dependency on the sputtering power, which can be explained by the bombardment flux and the incident kinetic energy to the target of the Ar ions. As the power increases, corresponding plasma current and target voltage also increase as can be seen in Figure 5-1. The increase of plasma current means the increase of the plasma density, namely the increase of the flux of incident Ar ions to the target. In addition, the kinetic energy of the incident Ar ions increases as the target voltage increases; thereby the sputtering yield increases and Mo atoms in the target are effectively sputtered. Thus, it is considered that the increase of the deposition rate is attributed to the combined effects of the increment of both number density and kinetic energy of Ar ions. It is also noted that the deposition rate increased with gas pressure; however, the increase is not significant at the pressure of above 0.3 mTorr, which is considered to be posed by scattering of Mo atoms, or "sputtering wind effect", or both.

Figure 5-3 shows the comparison of the obtained deposition rate with the model suggested by Ekpe *et al* [104]. The model assumes that the flux of sputtered atoms to the substrate only consists of fast atoms, and thermalized ones moving by diffusion is neglected. The flux of the fast atoms, ϕ is given by

$$\phi(pl) = \phi_{\mathrm{d}} \exp(-\zeta pl) \qquad \cdots\cdots\cdots (5.2)$$

$$\zeta \propto P^{-5/8} \qquad \cdots\cdots\cdots (5.3)$$

where p is the pressure, l is the distance between target and substrate, ζ is the parameter dependent on the free path of the atoms, P is the sputtering power, and ϕ_{d} is the initial flux emitted from the target. Good agreement is observed between experimental data and the model. It can be indicated that the deposition of the fast Mo atoms is the dominant mechanism in this system.

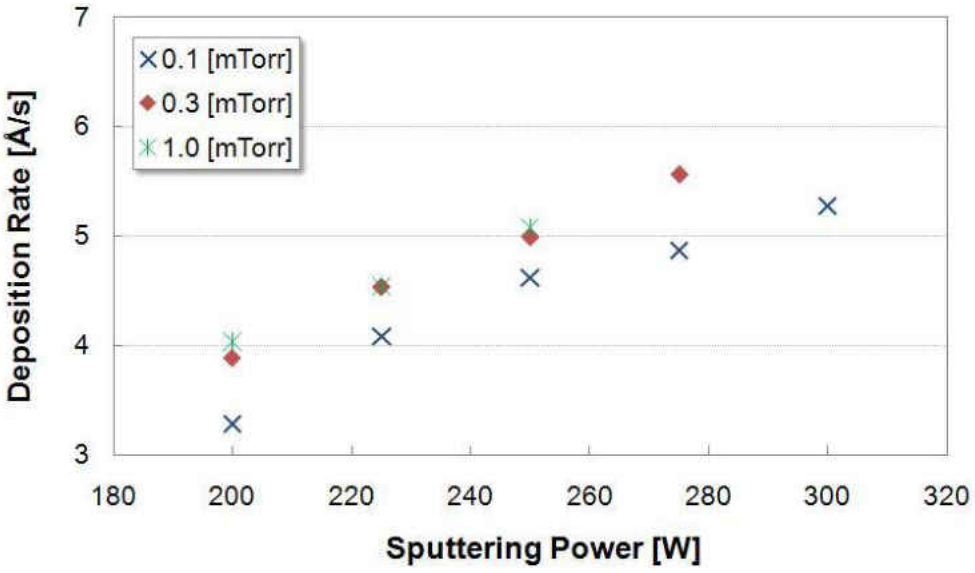

Figure 5-2: Variation in the deposition rate of Mo thin film with discharge power at 0.1, 0.3, and 1.0 mTorr

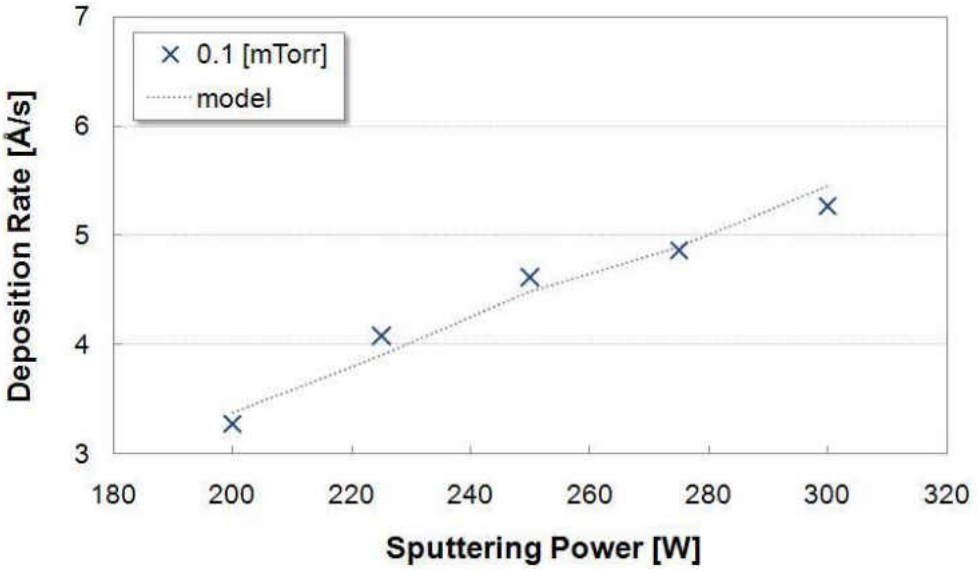

Figure 5-3: Comparison of deposition rate between the model [104] and experimental data

5.3 Crystal Structure

The crystallographic structure of Mo films was investigated using X-ray diffraction (XRD) technique in order to determine the influence of the preparation parameters on the crystallographic properties. Sputter-deposited films are polycrystalline in nature with body centered cubic (BCC) structure, and (110) plane is the closest-packed in BCC structure with the lowest surface energy.

5.3.1 Lattice Parameter

Figures 5-4 and 5-5 show the X-ray diffraction patterns of Mo thin films deposited at several pressures with the power of 200 W and 250 W, respectively. All spectra show the most intense peak at around 2θ=40.5˚ corresponding to ‹110› preferred orientation of BCC crystal. Table 5-2 summarizes the lattice parameters estimated from the Bragg's law, using (110) peak angle θ and wavelength of the Cu Kα X-ray λ.

The evaluated lattice parameters of the Mo films are ranging from 3.141 to 3.148 Å which is slightly smaller than the bulk value of 3.150 Å. This change in lattice parameter is attributed to the strain associated with the residual stress in the Mo thin film.

It is also noted that the peak intensity of (211) decreases with the gas pressure. This result indicates that the grains grow in not only ‹110› direction but also in ‹211› direction at lower pressures.

Table 5-2: Lattice parameters (unit: Å) of Mo thin films calculated from XRD (110) spectral peak and the wavelength of Cu Kα radiation

		Pressure [mTorr]			
		0.3	1.0	2.0	3.0
Power [W]	200	3.145	3.147	-	3.141
	250	3.147	3.148	3.146	-

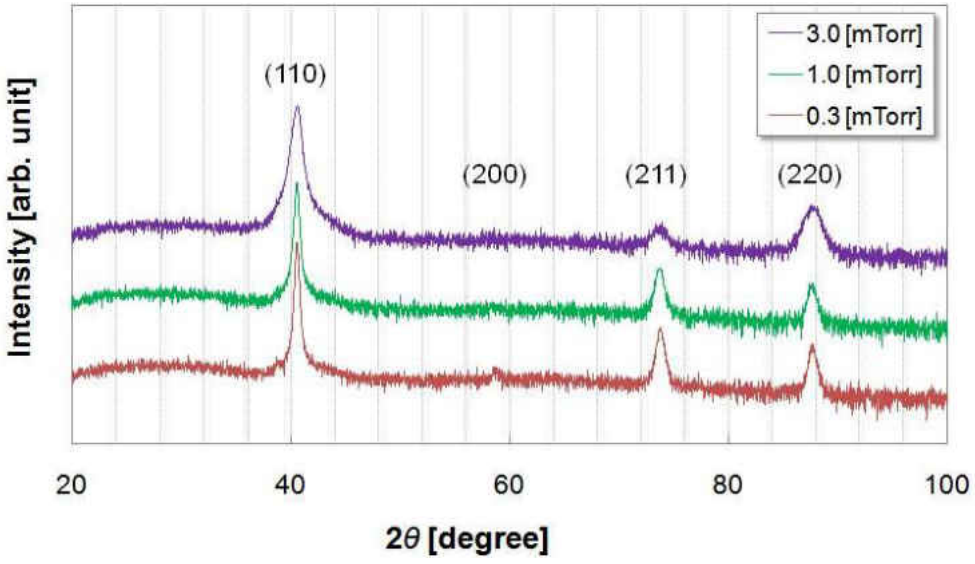

Figure 5-4: XRD spectrum patterns of Mo thin films deposited at 200 W and 0.3, 1.0, and 3.0 mTorr

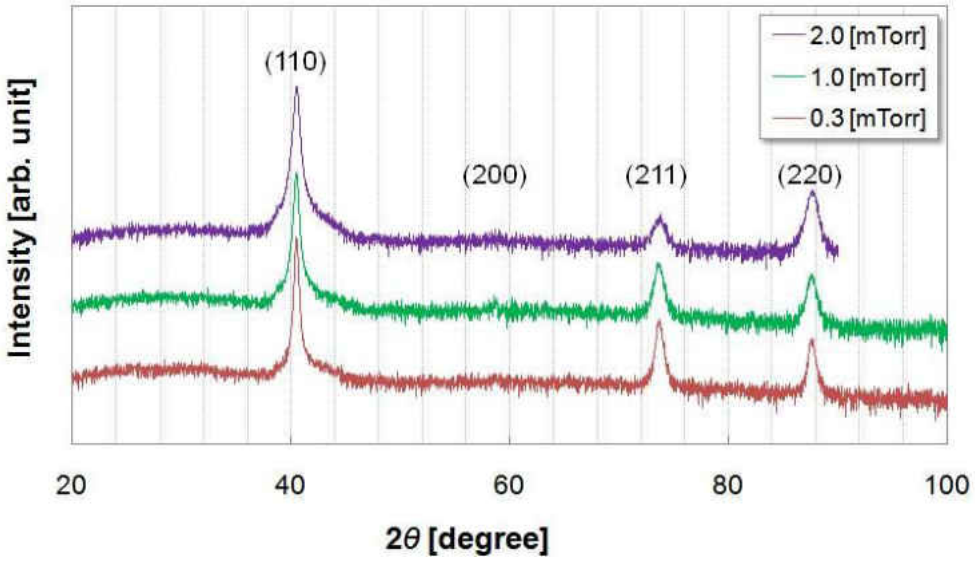

Figure 5-5: XRD spectrum patterns of Mo thin films deposited at 250 W and 0.3, 1.0, and 2.0 mTorr

5.3.2 Crystallinity

Figures 5-6 and 5-7 show the influence of the working gas pressure on the XRD (110) peak spectra of Mo thin films, where each spectrum is normalized with respect to the area under the curve so that all curves have same area of unity [11]. The diffraction patterns are all nearly smooth around the peak. Films with a broad peak are considered to have crystallized badly.

Since better crystallized material shows sharper spectrum peak, it can be indicated that the lower the working gas pressure, the better the crystal structure becomes. This result can be explained by the atomic peening effect. The kinetic energy of neutralized backscattering Ar atoms and sputtered Mo atoms are higher at lower gas pressure condition, which is associated with lower frequency of momentum transfer collision with back ground working gas atoms. The energetic incident atoms are considered to bring the films the atomic peening effect, and as a consequence, the films are densely packed and exhibit less defect concentration. Figure 5-8 also indicates the atomic peening effect caused by the higher target voltage. By increasing the power, thereby the target voltage, more energetic atom flux incidents the substrate and atomic peening effect is enhanced. Full width at half maximum (FWHM) for each peak is shown in Figure 5-9. The FWHM variation provides the quantitative information of the crystallinity discussed above. FWHM is influenced by defects, strain, and mean grain size in the film.

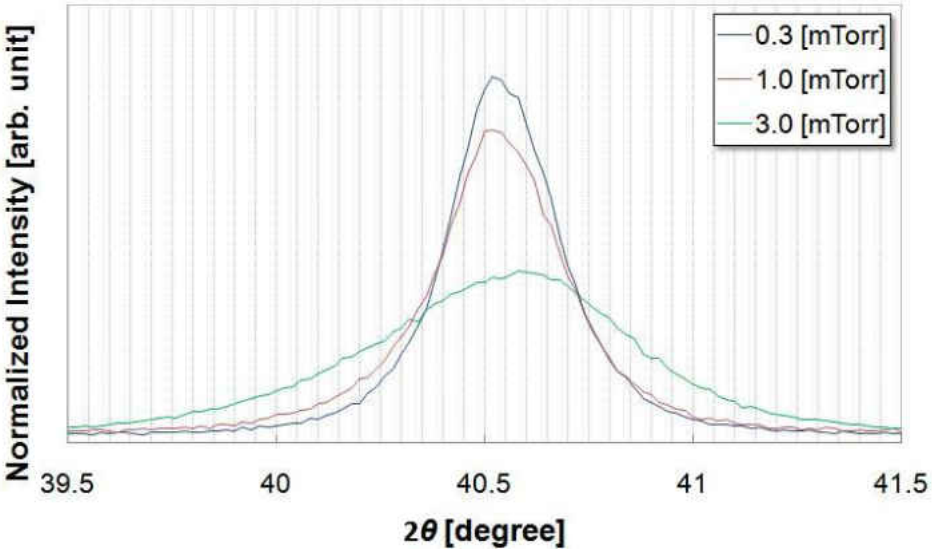

Figure 5-6: Normalized XRD profiles of (110) reflection peak of Mo thin films deposited at 200 W and 0.3, 1.0, and 3.0 mTorr

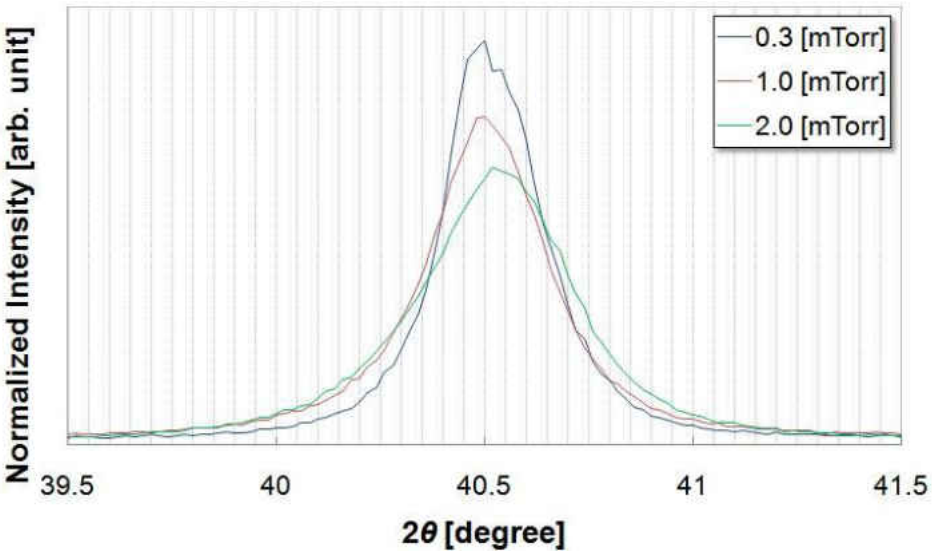

Figure 5-7: Normalized XRD profiles of (110) reflection peak of Mo thin films deposited at 250 W and 0.3, 1.0, and 2.0 mTorr

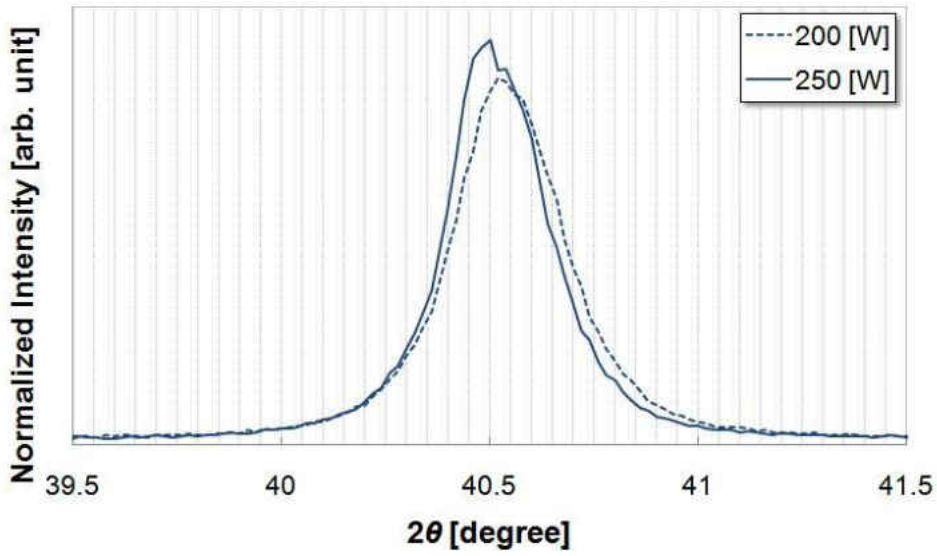

Figure 5-8: Comparison of XRD profiles of (110) reflection peak of Mo thin films between 200 W and 250 W (deposited at 0.3 mTorr)

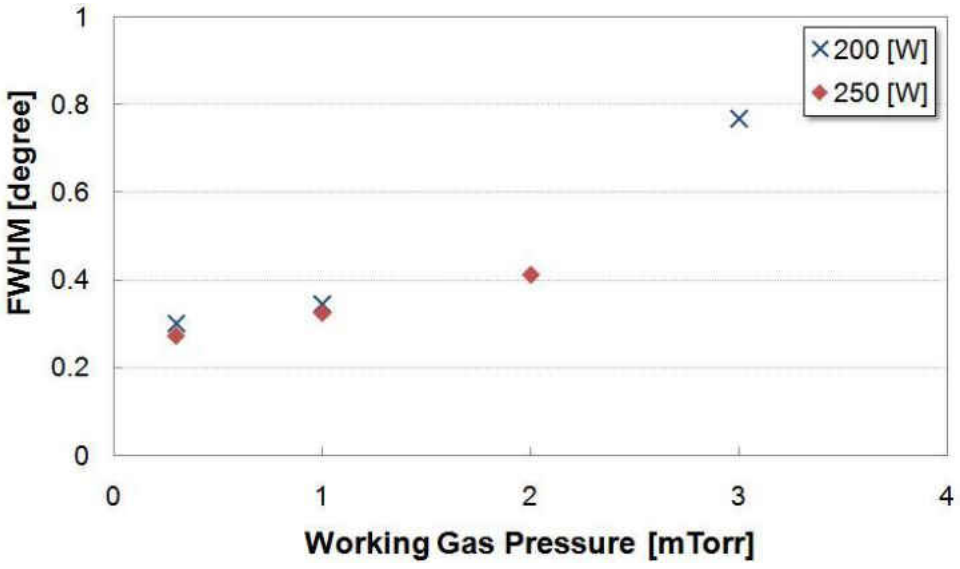

Figure 5-9: FWHM variation of Mo thin films (deposited at 200 and 250 W) as a function of working gas pressure

5.3.3 Grain Size

Mean grain size is estimated from FWHM of the diffraction peak using following Scherrer equation [105], [106], [107].

$$D = \frac{0.94\lambda}{W \cos\theta} \qquad \cdots\cdots\cdots (5.4)$$

where D is the mean grain size, λ is the X-ray wavelength, W is the FWHM measured in radians, and θ is the Bragg angle. It is important to keep in mind that the Scherrer equation is only applicable to grains smaller than about 1000 Å and inhomogeneous strain can also contribute to the width of a diffraction peak. Table 5-3 and Figure 5-10 show the relationship between working gas pressure and mean grain size of Mo films. The grain size of each film was found to increase from 115 to 325 Å by increasing the sputtering power and decreasing the gas pressure. It can be deduced that grain growth was facilitated by the atomic peening effect at lower pressure and higher power, hence grain coarsening occurred. The energetic incident atoms provide the energy to the Mo film to grow in ordered manner by striking the film surface as well as enhance the growth speed by providing the thermal energy, resulting in large grains and more intense (211) spectrum peaks observed at low pressure and high power condition.

Table 5-3: Mean grain size (unit: Å) of Mo thin films estimated from Scherrer equation

		Pressure [mTorr]			
		0.3	1	2	3
Power [W]	200	293	256	-	115
	250	325	272	214	-

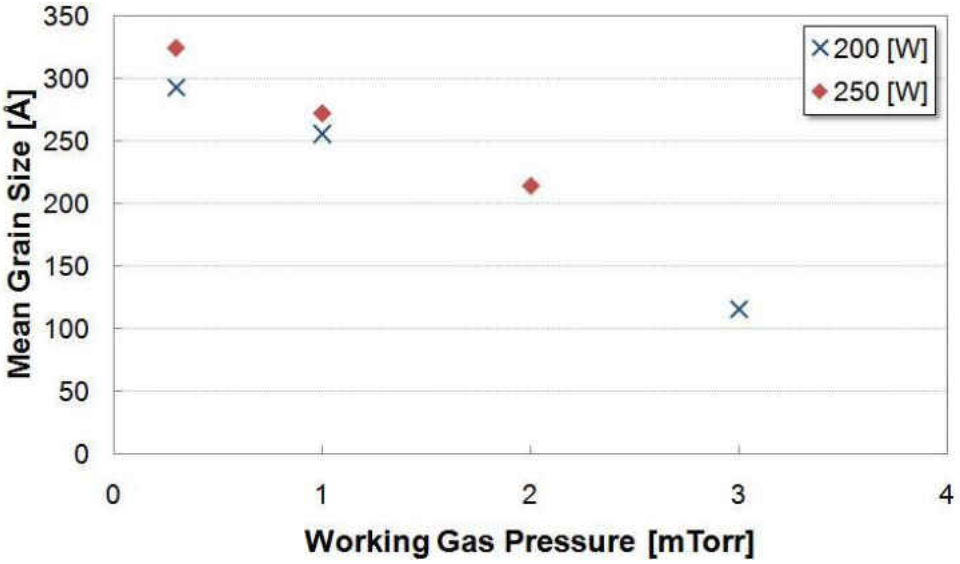

Figure 5-10: Mean grain size of Mo thin films (deposited at 200 and 250 W) estimated from Scherrer equation as a function of working gas pressure

5.4 Surface Morphology

Figures 5-11 and 5-12 shows the AFM images of the Mo thin films deposited at 200 and 250 W and gas pressure ranged from 0.3 to 3.0 mTorr. It can be seen that the grain size increases with increasing the sputtering power and decreasing the gas pressure. These images show very good consistency with the mean grain size evaluation using X-ray diffraction pattern in the previous section. Another attention should be paid to the shape of the grains. Grains become coarser when deposited at lower pressure, whereas grains at higher pressure tend to be more round and columnar.

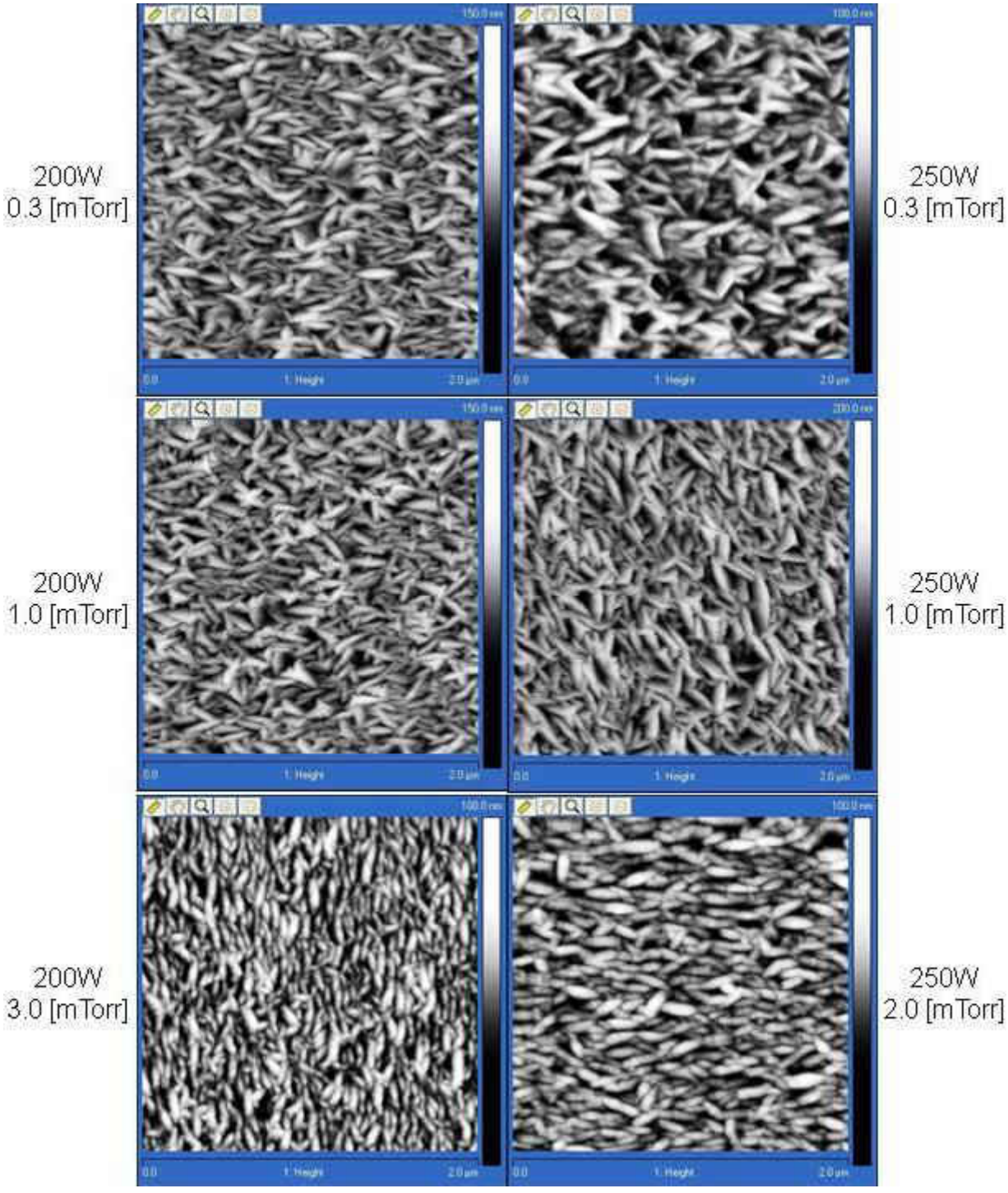

Figure 5-11: AFM images of Mo thin film surfaces at various sputtering conditions

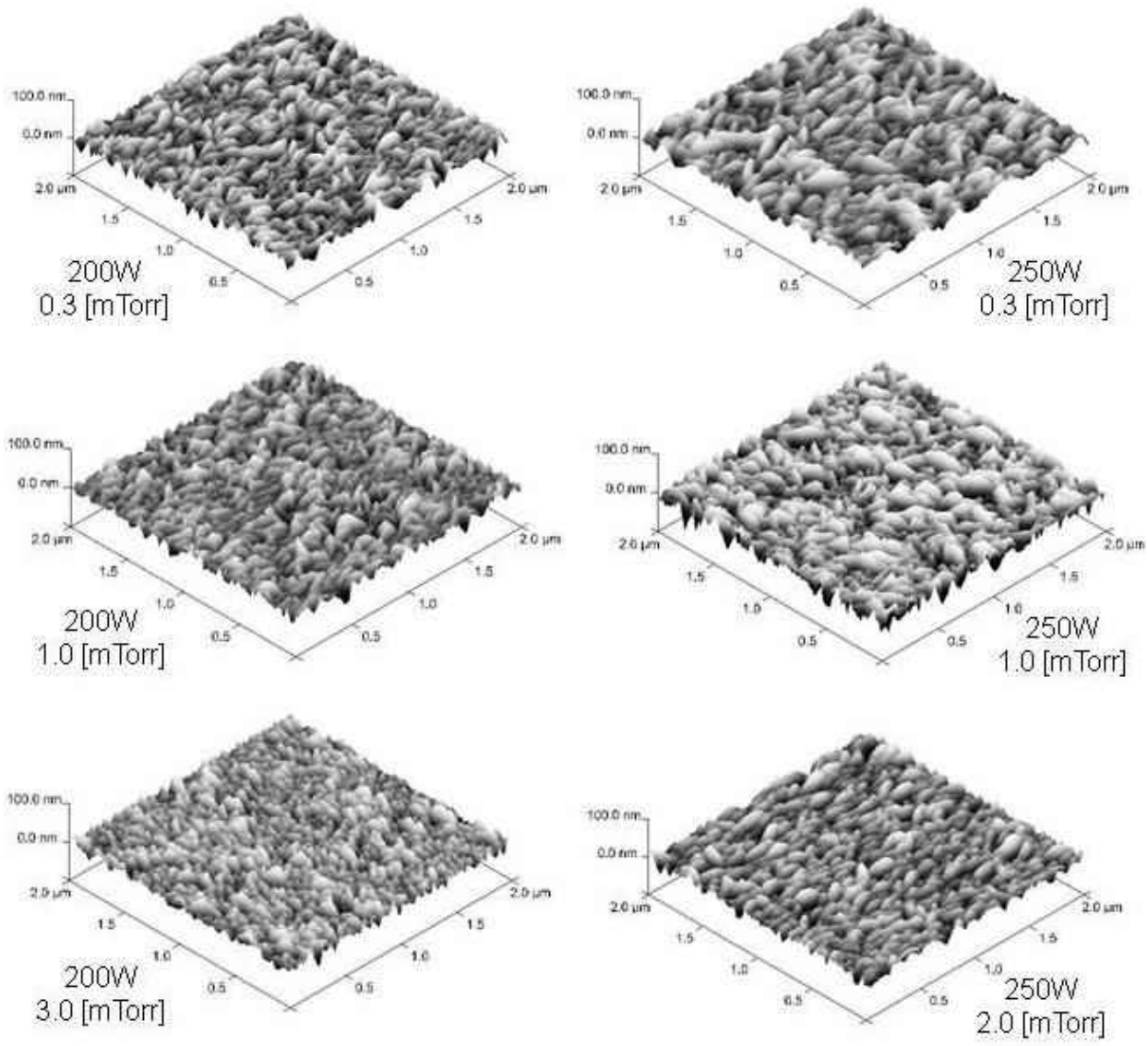

Figure 5-12: AFM images of Mo thin film surface roughness at various sputtering conditions

Figure 5-13 shows the influence of working gas pressure and sputtering power on the average surface roughness of the Mo thin films using Dektak profilometer. The results appear that the surface roughness is smoother at around 1.0 mTorr (11.5 to 14.5 Å) than at higher or

lower gas pressure conditions. However, low average roughness value is also observed at lower pressures despite the values are swinging between 13 to 26 Å at 0.1 mTorr.

Roughening at lower pressures is attributed to the coarse grains as mentioned in previous section. Whereas, at higher gas pressures, the films are suspected of having porous microstructure, voids, and cracks. If the gas pressure is higher, neutralized Ar and sputtered Mo atoms have more possibility to be scattered and arrive more obliquely at the substrate losing kinetic energy, resulting in slower grain growth with round columnar small grains. Further pressure increase is considered to pose "self-shadowing", resulting in porous and rougher surface as shown in Figures 5-11 and 5-12.

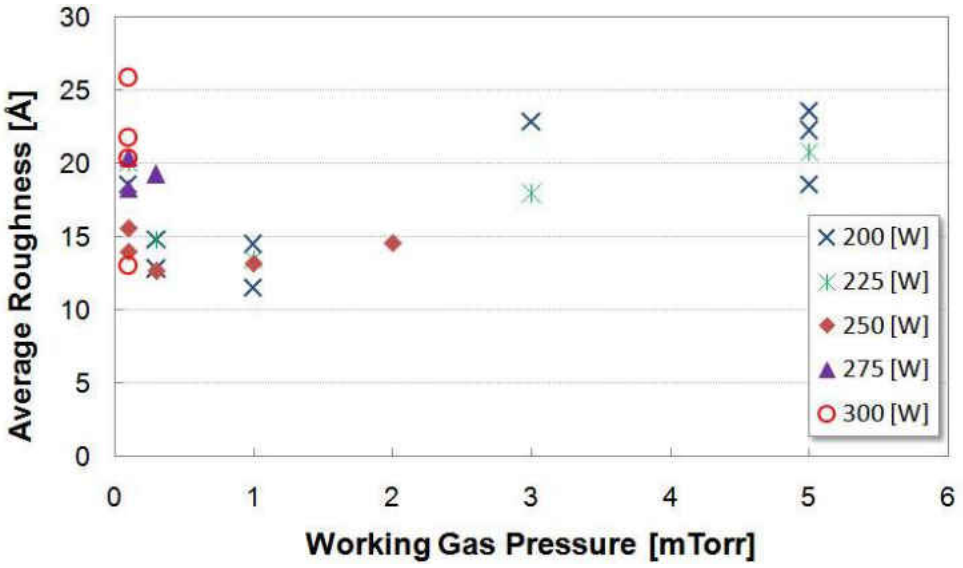

Figure 5-13: Variation of average roughness of Mo thin film surface (deposited from 200 W to 300 W) as a function of working gas pressure

5.5 Resistivity

Sheet resistance of the Mo thin films with thickness of about 7000 Å ranged from 0.036 to 7.53 Ω/sq at room temperature was obtained as shown in Figure 5-14. The resistivity at sputtering power of 200 W is shown in Figure 5-15 as a function of the working gas pressure. The resistivity of the Mo thin films is strongly influenced by the gas pressure, whereas sputtering power has much less influence compare to the gas pressure. When the pressure was 5 mTorr, the resistivity is in the range from 117 to 166 μΩ·cm, which is one order higher for the use as a back contact electrode layer of solar cells [11]. The lowest resistivity, 11.9 μΩ·cm was obtained in films prepared at a working gas pressure of 0.1 mTorr and a power of 250 W, which is roughly twice the room temperature bulk value of 5.4 μΩ·cm.

This difference in resistivity is explained by the relative oxygen and argon concentration in the films [105], [108]. G. Gordillo *et al*. reported that the reduction of the resistivity of the Mo films by reducing the working gas pressure is caused by an increase of both the Hall mobility and carrier concentration [30]. Resistivity data is a good indication of the combined effects of chemical impurities and physical defects in the Mo films on the movement of free electrons.

The resistivity curve shown in Figure 5-15 indicates a decreasing of structural defects with decreasing the working gas pressure. The observed increase in resistivity shown at higher gas pressure is deduced to be the direct result of the sputtering induced porosity mentioned in the earlier section. With decreasing the pressure, the probability of scattering of sputtered atoms becomes less, and the films become less porous and more tightly packed. This tightly packed microstructure results in the decrease of film resistivity.

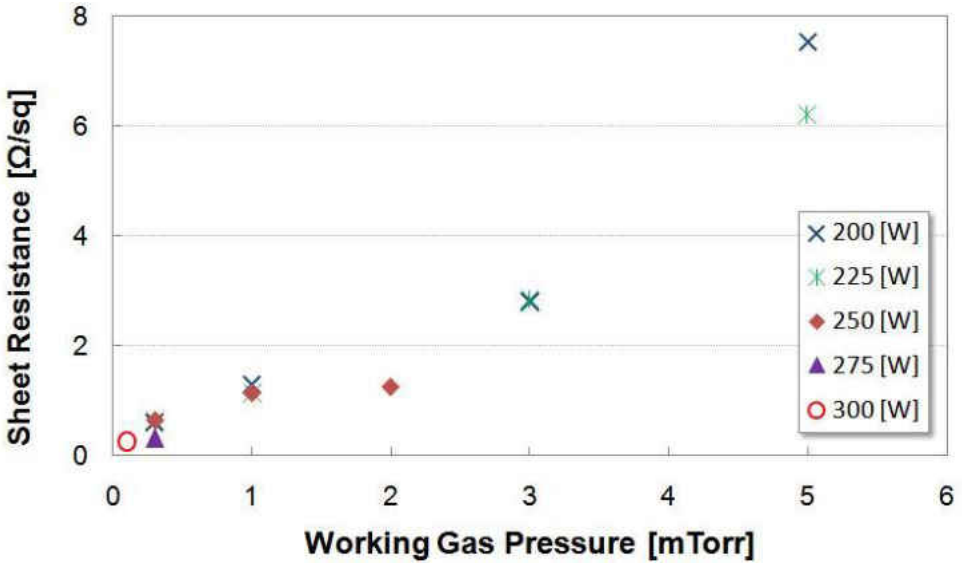

Figure 5-14: Sheet resistance variation of Mo thin films with thickness of about 7000 Å as a function of working gas pressure

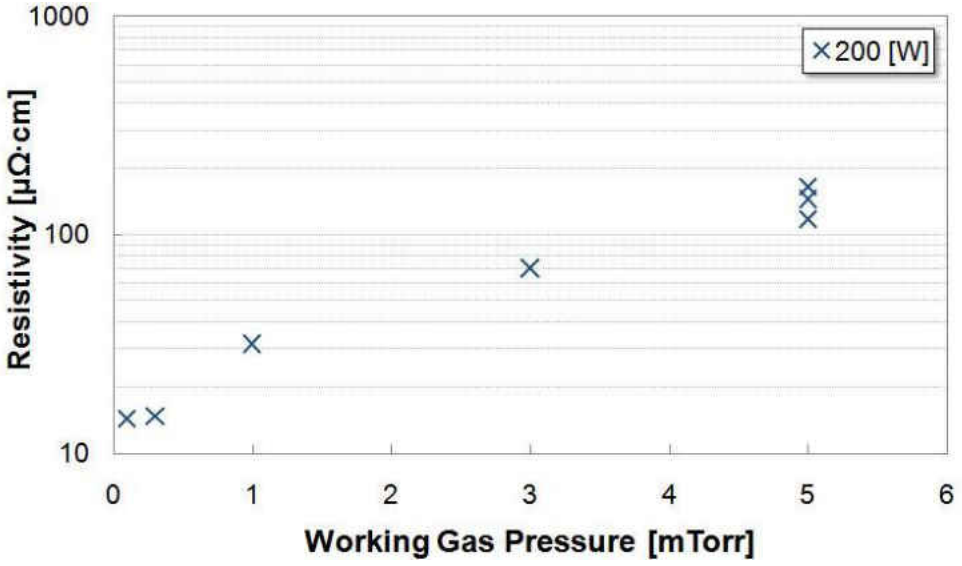

Figure 5-15: Resistivity variation of Mo thin films as a function of working gas pressure (deposited at 200W)

Figure 5-16 shows the correlation between resistivity and the average grain size. It clearly indicates that the resistivity decreases with increasing the grain size through the decrement of the working gas pressure. The smaller the mean grain size is, the more the grain boundaries exist, thereby, the resistivity increases with decreasing the mean grain size. However, the films deposited at lower power exhibit lower resistivity even though they have smaller grains than that of the films deposited at higher power. This phenomenon can be considered to be caused by the incorporation of Ar atoms within the Mo thin films [20].

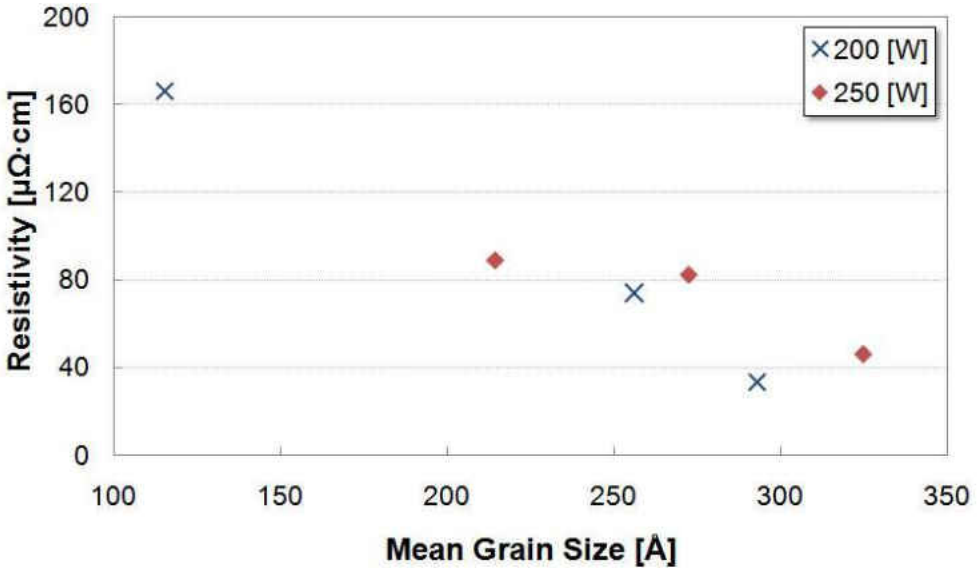

Figure 5-16: Resistivity variation of Mo thin film as a function of mean grain size (deposited at 200 and 250 W)

5.6 Stress Analysis

Bent very thin glass strips by the film deposition were used to estimate the amount of stress present in the Mo thin films. This was a crude approach for qualitative understanding of the stress build up by varying the deposition parameters. After unloaded from the sputtering system, the deflection at the end of the glass strip, δ was measured. Figure 5-17 shows a typical image of the glass strips bent by the deposition. When the residual stress of the film is compressive, the glass strip bends toward the other side of the deposited face. On the other hand, if the film is in tensile state, the glass strip bends toward the deposited face. As indicated in equation (4.2), the magnitude of the deflection is proportional to the amount of stress, therefore the higher the deflection a glass strip shows, the higher the residual stress of the film is.

Figure 5-17: Image of a bent glass strip

The residual stresses in Mo films deposited by DC magnetron sputtering system are shown in Figure 5-18 as a function of target voltage. The films were deposited at 0.1 mTorr. A monotonous decrease in tensile stress from 322 MPa at 290 V to 152 MPa at 316 V is observed with increasing the target voltage. This result can again be explained in terms of atomic peening

effect [109], namely, the kinetic energy of incident backscattering neutralized Ar atoms and Mo adatoms to the substrate. These energetic particles also limit the development of a columnar morphology growth by coarsening as mentioned earlier. These effects lead the deposited films to the densification in microstructure.

At lower target voltages, the kinetic energy of the incident Ar ions to the Mo target is less, resulting in less kinetic energy of sputtered Mo atoms and neutralized backscattering Ar atoms. Due to the lack of the energy necessary to arrange the atoms in ordered manner, obtained microstructure is characterized by porous columnar grain growth and a number of defects.

Attractive force strength, which is responsible for tensile stress, among grains or atoms is inversely proportional to the intergranular or interatomic spacing. Thus, with decreasing the target voltage, the films developed a tensile stress with increasing the intergranular spacing, and reversely, increasing the discharge voltage results in decrement of the number of open site inside the film, and thereby reduces the tensile stress. The round columnar grains observed for the tensile stress films imply the presence of micro-voids inside the material. The inner surface of the voids has the high surface tension which tries to shrink the film. Hence, less tensile stressed film is obtained by increasing the discharge power.

Figure 5-19 shows the residual stress of Mo films deposited at 200 W as a function of working gas pressure. If film is deposited at higher pressures, it can be expected that collisions with background Ar gas atom reduce the kinetic energy of sputtered Mo atoms and reflected neutral Ar gas atoms, resulting in more porous and less densely packed Mo film with significant

tensile stress state. The discussion is true below the gas pressure of 0.3 mTorr; however, further increase of gas pressure results in attenuation of the tensile stress down to zero.

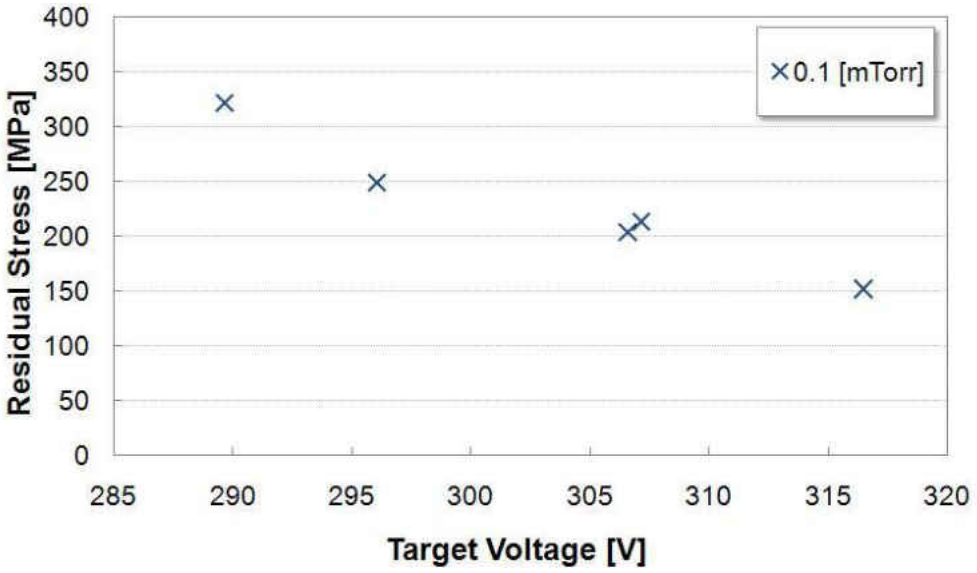

Figure 5-18: Residual stress variation of Mo thin film as a function of discharge voltage at 0.1 mTorr

This tensile stress reduction can be explained by the model proposed by Müller [110] who simulated the micro structures of thin films with two-dimensional (2D) molecular dynamics. Residual tensile stress is related to the defect and void size distribution; however, the intergranular attractive force works effectively only when the void size is smaller than a certain critical size. Itoh *et al*. reported quantitatively the tensile stress reduction at higher pressure by inter atomic force depicted in Figure 5-20 in the case of body centered cubic structure [111].

The mechanism is explained as follows. The increment of working gas pressure imposes the sputtered Mo atom more chance to be scattered by the gas atoms. Sputtered Mo atoms are losing their kinetic energy on the way to the substrate. Less energetic incident Mo adatoms tend to develop less ordered and loosely packed grains with porous microstructure. Backscattered Ar atoms become less energetic in the same manner as Mo atom, and cannot contribute to the formation of the dense microstructure. In addition, the angle at which adatoms incident to the substrate becomes more oblique, which causes self-shadowing effect and nourish porous microstructure. Hence, resulting Mo films become less tensile due to the excessively porous microstructure.

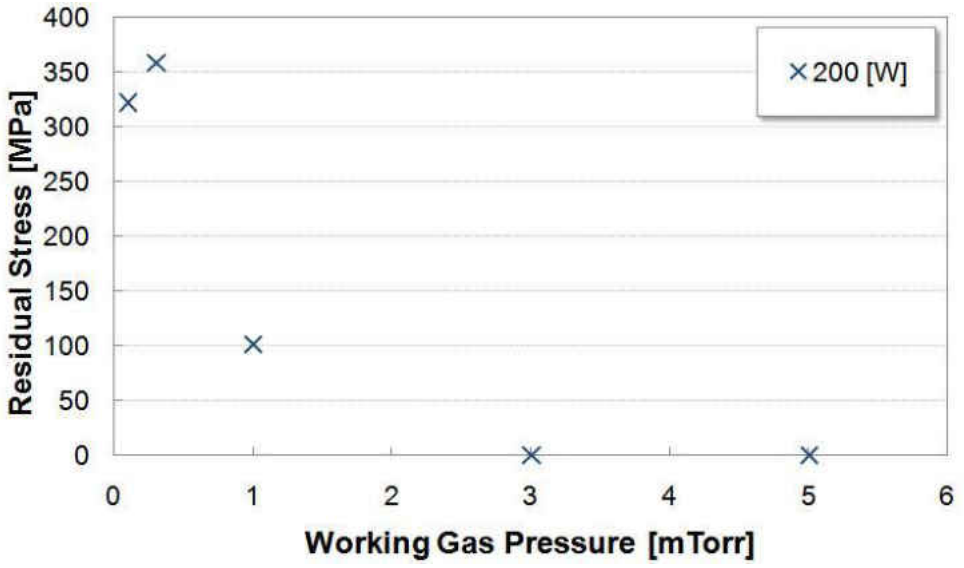

Figure 5-19: Residual stress variation of Mo thin films deposited at 200 W as a function of working gas pressure

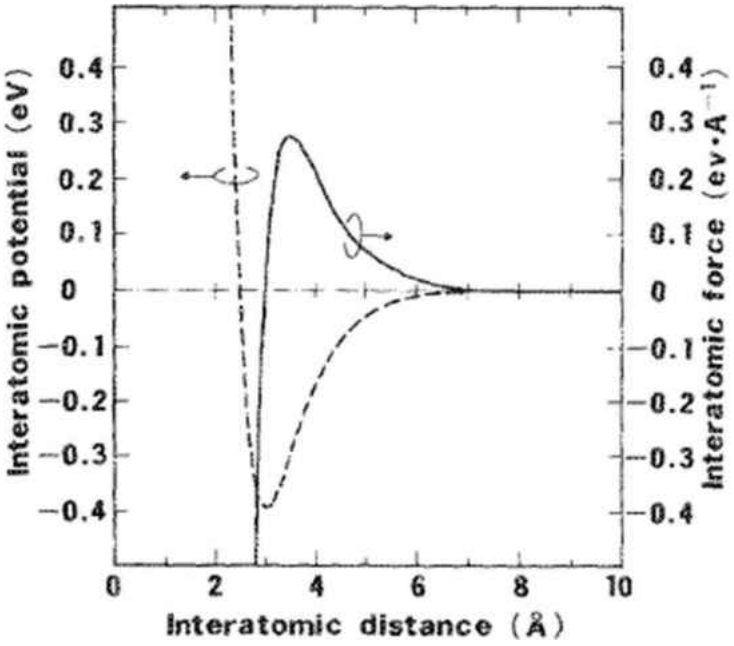

Figure 5-20: Interatomic potential and force of tungsten [111]

Mean free path of sputtered Mo atoms with Ar background gas shown in Figure 5-21 endorses the stress state change at higher gas pressure [112]. From molecular dynamics theory, the mean free path, λ of sputtered atom with mass M_s is given by [113]

$$\frac{1}{\lambda} = \pi \frac{p}{kT} \left(r_s + r_g\right)^2 \sqrt{1 + \frac{M_s}{M_g}} \qquad \cdots\cdots\cdots (5.5)$$

where p and M_g are the partial pressure and mass of the background gas, r_s and r_g are the radii of sputtered atom and background gas atom, respectively. According to Figure 5-21, mean free path dramatically reduces from 166 mm at 0.3 mTorr to 50 mm at 1.0 mTorr. A sputtered Mo atom at 0.1 mTorr has almost no chance to reduce its kinetic energy by collision and is directly incident to the substrate, whereas a sputtered atom at 1.0 mTorr has a higher probability of collision with

background gas atom. It is estimated that Mo atoms collide with Ar background gas atom roughly twice by the time it reaches the substrate. This significant difference in mean free path between the two pressure conditions makes the stress state change. In addition, at 0.1 mTorr, sputtered atoms incident to the substrate almost normally, whereas at 1.0 mTorr, most of the atoms are scattered and incident to the substrate at oblique angle. Incidence at oblique angle can cause self-shadowing during the film growth [92], resulting in extremely porous microstructure which is responsible for the loss of intergranular attractive force, thereby tensile stress state.

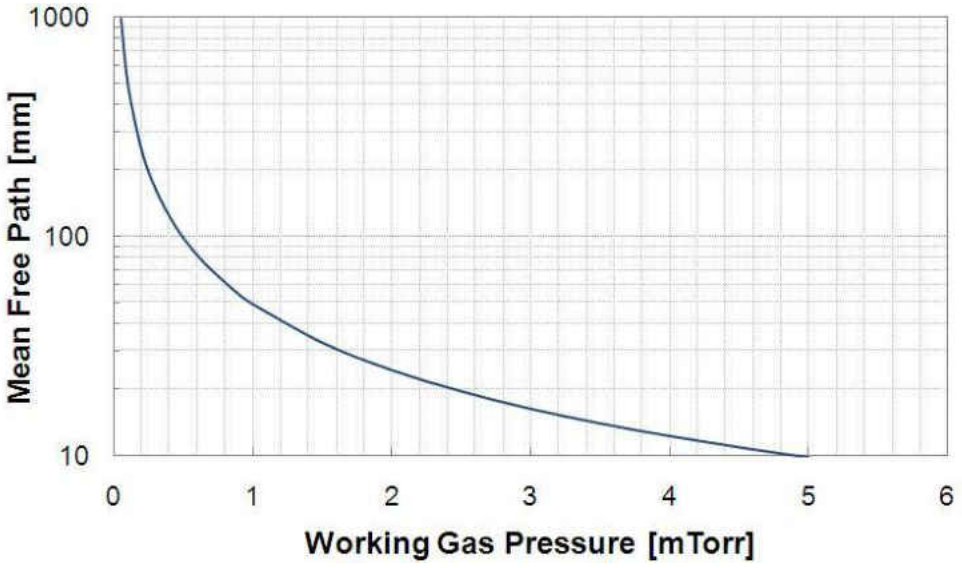

Figure 5-21: Variation of mean free path of sputtered Mo atom as a function of working gas pressure

When the intergranular spacing decreases so that grains begin to push one another, compressive forces associated with repulsive force begin to exceed the above mentioned attractive force. It has been reported that compressive forces stem from the incorporation of

oxygen, hydrogen and water vapor for a variety of metallic and dielectric thin films [24], [114], [115]. However, compressive stress state was not obtained with the system employed in this investigation.

5.7 Kinetic Energy of Incident Atoms

From the above mentioned discussions, it can be deduced that the kinetic energy of incident atoms determines the microstructure. Atoms collide with background gas atoms during the transport to the substrate with losing the kinetic energy. Kinetic energy of the incident atom is given by [104]

$$E_{\text{in}} = E_{\text{out}} \exp\left(-\frac{\sigma p l}{kT}\right) \qquad \cdots\cdots\cdots (5.6)$$

where E_{in} is the kinetic energy of the incident atom, E_{out} is the initial kinetic energy of the atom, l is the distance between the substrate and the target, and σ is the cross section for momentum transfer collision with background gas atom. According to equation (5.6), the kinetic energy of incident atom is proportional to $\exp(-cp)$ if other terms are fixed, where c is a constant. Thereby,

$$E_{\text{in}} = V\exp(-cp) \qquad \cdots\cdots\cdots (5.7)$$

where target voltage,V is assumed to equal to E_{out}. Thus, the kinetic energy of incident atoms can be represented by this pseudo-kinetic energy, E_{in}.

5.7.1 Influence of Kinetic Energy on Residual Stress

Figure 5-22 shows the re-plotted all residual stress data against pseudo-kinetic energy. It can be considered that intergranular spacing is determined by kinetic energy of incident atoms. In other words, stress state of the deposited Mo film has a strong correlation with kinetic energies of incident atoms.

As expected, the data shows the strong correlation between kinetic energy of incident atom and residual stress. The reduction of tensile stress at higher energy region is much steeper than lower energy region. It is noted that further increase of kinetic energy via reducing the gas pressure or increasing the target voltage may result in compressive stress which may peel off a Mo thin film from the glass substrate. Therefore, pseudo kinetic energy should be less than 300.

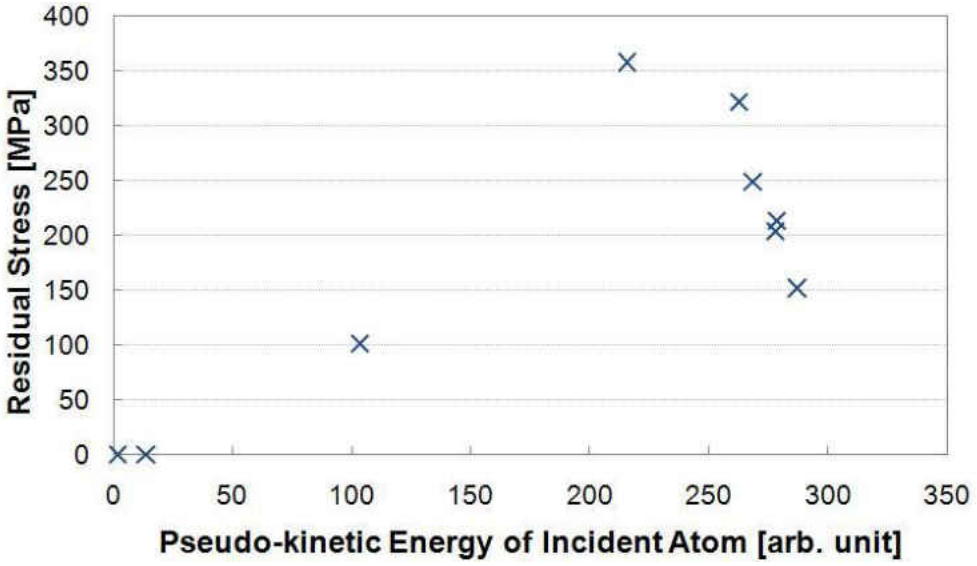

Figure 5-22: Residual stress variation of Mo thin film as a function of pseudo-kinetic energy of incident atoms

5.7.2 Influence of Kinetic Energy on Surface Morphology

Figures 5-23 shows the average roughness as a function of pseudo-kinetic energy. The roughening at the higher energy region is considered to be due to the coarsening originated from the atomic peening effect. However, the region where target voltage is higher than 300 V shows swings. On the other hand, the roughening at lower energy region below 50 is deduced to stem from poor microstructural characteristics such as micro voids and micro cracks. Thus, pseudo-kinetic energy should be more than 50, and target voltage should be less than 300 V to achieve a controllable surface morphology.

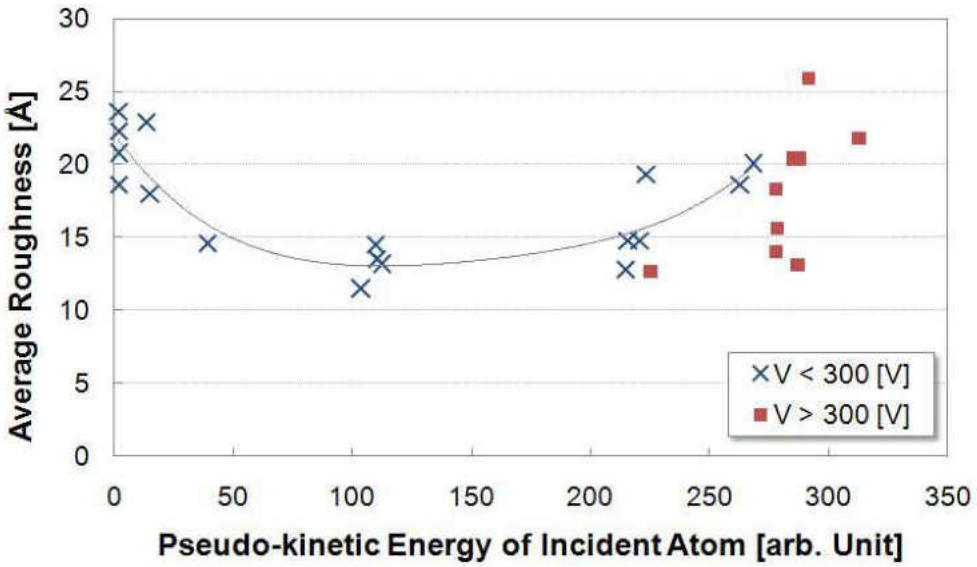

Figure 5-23: Average roughness variation of Mo thin film as a function of kinetic energy of incident atoms

5.8 Adhesion

All the films deposited in this investigation passed the Scotch-tape test. It has been reported that Mo films in compressive stress adhere poorly to the glass substrate, and those in tensile stress have a good adhesion. Since the films obtained in this investigation are all in tensile stress state, they are considered to exhibit a good adherence to the glass substrate.

CHAPTER 6 CONCLUSIONS AND RECOMMENDATIONS

Variety of properties of Mo thin films prepared by DC magnetron sputtering under different process parameters has been investigated. The results showed following influences of working gas pressure and discharge power on properties of Mo thin film.

6.1 Deposition Rate

Deposition rate showed strong correlation with discharge power of the sputtering system. Deposition rate of 3.3 Å/s was obtained at 200 W, and the deposition rate increased up to 5.6 Å/s by increasing the power up to 300 W. Increase of the power originates from increase of both plasma current and discharge voltage. High plasma current is attributed to high discharge rate, namely high number of Ar ion, and effective sputtering of Mo atom is achieved by energetic Ar ion due to high discharge voltage. Hence, deposition rate increases with increasing discharge power.

Deposition rate does not increase with increasing the working gas pressure despite the plasma current increases. The number of sputtered Mo atom increases with increasing the gas pressure; however, the high scattering rate invoked by the high gas pressure diminish the number of Mo atoms arriving at the substrate. Hence, the effect of increase of gas pressure on deposition rate is compensated.

6.2 Residual Stress

Residual stress state was found to be strongly dependent on the kinetic energy of incident Mo atoms and backscattered Ar atoms to the substrate. At lower gas pressure and higher discharge voltage, incident atoms are more energetic and incident to the substrate normally because of their longer mean free path and higher flying speed. These energetic incident atoms cause the atomic peening effect, resulting in densely packed microstructure. Hence, less tensile or compressive films are obtained.

By increasing the gas pressure or decreasing the voltage, incident atoms become less energetic and atomic peening diminishes. As a result, intergranular and interatomic spacing increase to develop tensile stress which is exerted by attractive force among the grains and atoms.

Further increment of pressure or decrement of voltage makes the film more porous. When the spacing excesses certain value so that the attractive force does not reach, eventually, the film exhibits no stress. Especially at higher pressures, since atoms have higher probability to be scattered by back ground gas, the incident angle tends to become oblique. The oblique incidence poses self-shadowing which enhances porous film growth more.

6.3 Resistivity

Resistivity was found to depend on working gas pressure. Low resistivity ranging from 11.9 to 14.4 μΩ·cm was obtained at 0.1 mTorr within 200 and 300 W. The lowest value of 11.9

μΩ·cm was obtained under 250 W and 0.1 mTorr. Since atoms are densely packed and grains are large and less defective due to the atomic peening effect below the pressure of 0.3 mTorr, films tend to be less resistive. Results also indicated the existence of incorporated Ar inside the Mo thin film under higher discharge power condition.

6.4 Morphology

Coarser grains tend to grow at lower gas pressure and higher sputtering voltage conditions, which make the film surface rougher. Whereas round columnar grains with porous microstructure are observed at higher pressure and lower voltage conditions.

6.5 Suggested Future Work

To achieve a highly conductive Mo thin film, lowering the gas pressure less than about 0.3 mTorr is the essential condition according to the results. On the other hand, the kinetic energy of incident atoms to the substrate also has to be controlled for appropriate surface morphology by setting the pseudo-kinetic energy more than 50 and target voltage less than 300 V. Compressive stress is absolutely not good for a good adhesion, therefore, pseudo-kinetic energy has to be less than 300 to avoid peeling off. Given these restrictions, Table 6-1 shows the potential process parameters that achieve highly conductive, well adhesive, and appropriate-surfaced Mo thin film back contact layer for CIGS solar cells.

For future work, it is recommended to fabricate CIGS solar cells on the Mo back contact thin film layers deposited with the conditions picked up from Table 6-1 to examine the influence of surface morphology and microstructure on grain growth of CIGS absorber and solar cell performance, and stability of adhesive strength throughout the fabrication process.

Table 6-1: Suggested sputtering deposition conditions that achieve qualified Mo thin film single layer for CIGS solar cells

		Target Voltage [V]					
		250	260	270	280	290	300
Working Gas Pressure [mTorr]	0.05	110	129	151	175	202	233
	0.1	108	127	149	173	201	232
	0.15	106	125	147	172	199	231
	0.2	103	123	145	170	198	229
	0.25	101	120	143	168	196	228
	0.3	99	118	141	166	195	227
		Sputtering Power [W]					

LIST OF REFFERENCES

[1] "World energy outlook: Executive summary," Paris, France: International Energy Agency, 2009. [online]. Available: http://www.worldenergyoutlook.org/docs/weo2009/WEO2009_es_english.pdf

[2] S. Shafiee and E. Topal, "When will fossil fuel reserves be diminished?" *Energy Policy*, vol. 37, pp. 181-189, 2009.

[3] P.K. Dutta, R. Radner, "A strategic analysis of global warming: Theory and some numbers," *Journal of Economic Behavior and Organization*, vol. 71, pp. 187-209, 2009.

[4] N. Kulkarni and J. Grigg, "Effect of air pollution on children," *Paediatrics and Child Health*, vol. 18, pp. 238-243, 2008.

[5] L.L. Kazmerski, "Photovoltaics: A review of cell and module technologies," *Renewable and Sustainable Energy Reviews*, vol. 1, pp. 71-170, 1997.

[6] "*Global market outlook for photovoltaics until 2013*," Brussels, Belgium: European Photovoltaic Industry Association, April 2009. [online]. Available: http://www.asif.org/files/EPIA_Perspectiva_del_Mecado_FV_Global_hasta_2013.pdf

[7] Arvind Chel and G.N. Tiwari, "Stand-alone photovoltaic (PV) integrated with earth to air heat exchanger (EAHE) for space heating/cooling of adobe house in New Delhi (India)," *Energy Conversion and Management*, vol. 51, pp. 393-409, 2010.

[8] V. Fthenakis, "Sustainability of photovoltaics: The case for thin-film solar cells," *Renewable and Sustainable Energy Reviews*, vol. 13, pp. 2746-2750, 2009.

[9] I. Repins, M.A. Contreras, B. Egaas, C. DeHart, J. Scharf, C.L. Perkins, B. To, and R. Noufi, "19.9%-efficient ZnO/CdS/$CuInGaSe_2$ solar cell with 81.2% fill factor," *Progress in Photovoltaics: Research and Applications*, vol. 16, pp. 235-239, 2008.

[10] M.A. Green, K. Emery, Y. Hishikawa, and W. Warta, "Solar cell efficiency tables (version 35)," *Progress in Photovoltaics: Research and Applications*, vol. 18, pp. 144-150, 2010.

[11] J.H. Scofield, A. Duda, D. Albin, B.L. Ballard, and P.K. Predecki, "Sputtered molybdenum bilayer back contact for copper indium diselenide-based polycrystalline thin-film solar cells," *Thin Solid Films*, vol. 260, pp. 26-31, 1995.

[12] F.A. Abou-Elfotouh, L.L. Kazmerski, R.J. Matson, D.J. Dunlavy, and T.J. Coutts, "Studies of the electrical and interface properties of the metal contacts to $CuInSe_2$ single crystals," *Journal of Vacuum Science and Technology A*, vol. 8, pp. 3251-3254, 1990.

[13] S. Ashour, S. Alkuhaimi, H. Moutinho, R. Matson, and F. Abou-Elfotouh, "Junction formation and characteristics of CdS/$CuInSe_2$/metal interfaces," *Thin Solid Films*, vol. 226, pp. 129-134, 1993.

[14] F.A. Abou-Elfotouh, L.L. Kazmerski, T.J. Coutts, R.J. Matson, S.E. Asher, A.J. Nelson, and A.B. Swartzlander-Franz, "Interface properties of (Cd,Zn)S/CuInSe2 single-crystal solar cells," *Journal of Vacuum Science and Technology A*, vol. 7, pp. 837-841, 1989.

[15] R.J. Matson, O. Jamjoum, A.D. Buonaquisti, P.E. Russell, L.L. Kazmerski, P. Sheldon, and R.K. Ahrenkiel, "Metal contacts to $CuInSe_2$," *Solar Cells*, vol. 11, pp. 301-305, 1984.

[16] E. Moons, T. Engelhard, D. Cahen, "Ohmic contacts to p-$CuInSe_2$ crystals," *Journal of Electronic Materials*, vol. 22, no. 3, pp. 275-280, 1993.

[17] D.W. Niles *et al*., *Materials Research Society Symposium Proceedings*, vol. 260, p. 299, 1992.

[18] L. Assmann, J.C. Bernède, A. Drici, C. Amory, E. Halgand, and M. Morsli, "Study of the Mo thin films and Mo/CIGS interface properties," *Applied Surface Science,* vol. 246, pp. 159-166, 2005.

[19] J.A. Thornton and D.W. Hoffman, "Stress-related effects in thin films," *Thin Solid Films*, vol. 171, pp. 5-31, 1989.

[20] D.W. Hoffman and J.A. Thornton, "Internal stresses in Cr, Mo, Ta, and Pt films deposited by sputtering from a planar magnetron source," *Journal of Vacuum Science and Technology*, vol. 20, pp. 355-358, 1982.

[21] J.A. Thornton and D.W. Hoffman, "The influence of discharge current on the intrinsic stress in Mo films deposited using cylindrical and planar magnetron sputtering sources," *Journal of Vacuum Science and Technology A*, vol. 3, pp. 576-579.

[22] T.J. Vink, M.A.J. Somers, J.L.C. Daams, and A.G. Dirks, "Stress, strain, and microstructure of sputter-deposited Mo thin films," *Journal of Applied Physics*, vol. 70, pp. 4301-4308, 1991.

[23] K. Orgassa, H.W. Schock, and J.H. Werner, "Alternative back contact materials for thin film Cu(In,Ga)Se2 solar cells," *Thin Solid Films*, vol. 431-432, pp. 387-391, 2003.

[24] T. Yamaguchi and R. Miyagawa, "Effects of oxygen on the properties of sputtered molybdenum thin films," *Japanese Journal of Applied Physics*, vol. 30, pp. 2069-2073, 1991.

[25] B.L. Ballard, P.K. Predecki, D. Albin, and J.H. Scofield, *Advance in X-ray Analysis*, vol. 38, 1994.

[26] K. Granath *et al.*, in *Proceedings of the 13th European Photovoltaic Solar Energy Conference*, 1995, p. 1483.

[27] R. Menner, E. Gross, A. Eicke, H. Dittrich, J. Springer, B. Dimmler, U. Rühle, M. Kaiser, T. Magorian-Friedlmeier, and H.W. Schock, "Investigations on sputter deposited molybdenum back contacts for Cu(In,Ga)Se_2," in *Proceedings of the 13th European Photovoltaic Solar Energy Conference*, 1995, p. 2067.

[28] B.C. Bell and D.A. Glocker, "The effect of initial growth conditions on the stress profiles of Mo sputtered onto both moving and stationary substrates," *Journal of Vacuum Science and Technology A*, vol. 10, no. 4, pp. 1442-1445, 1992.

[29] Y.G. Shen, "Effect of deposition conditions on mechanical stresses and microstructure of sputter-deposited molybdenum and reactively sputter-deposited molybdenum nitride films," *Materials Science and Engineering A*, vol. 359, pp. 158-167, 2003.

[30] G. Gordillo, M. Grizález, and L.C. Hernandez, "Structural and electrical properties of DC sputtered molybdenum films," *Solar Energy Materials and Solar Cells*, vol. 51, pp. 327-337, 1998.

[31] J. Zhao, A. Wang, and M.A. Green, "19.8% efficient "honeycomb" textured multicrystalline and 24.4% monocrystalline silicon solar cells," *Applied Physics Letters*, vol. 73, pp. 1991-1993, 1998.

[32] M.A. Green, *Solar Cells: Operating Principles, technology, and System Applications*, Englewood, NJ: Prentice-Hall, 1982.

[33] R.S. Muller, T.I. Kamins, and M. Chan, *Device Electronics for Integrated Circuits*, 3rd ed. Hoboken, NJ: John Wiley & Sons, 2002

[34] A. Luque and S. Hegedus, Ed., *Handbook of Photovoltaic Science and Engineering*, England: John Wiley and Sons, 2003.

[35] B. Dimmler, H. Dittrich, R. Menner, and H.W. Schock, "Performance and Optimization of Heterojunctions Based on Cu(Ga,In)Se_2", in *Proceedings of 19th IEEE Photovoltaic Specialist Conference*, 1987, p. 1454.

[36] C. Rincón and J. González, "Temperature dependence of the bandgap in $CuInSe_2$", *Solar Cells*, vol.16, pp. 357-362, 1986.

[37] L.L. Kazmerski, M. Hallerdt, J. Ireland, R.A. Mickelsen, and W.S. Chen, "Optical properties and grain boundary effects in $CuInSe_2$," *Journal of Vacuum Science and Technology A*, vol. 1, pp. 395-398, 1983.

[38] A. Jasenek, U. Rau, K. Weinert, I.M. Kötshau, G. Hanna, G. Voorwinden, M. Powalla, and H.W. Werner, "Radiation resistance of Cu(In,Ga)Se2 solar cells under 1-MeV electron irradiation," *Thin Solid Films*, vol. 387, pp. 228-230, 2001.

[39] J.F. Guillemoles, "Stability of Cu(In,Ga)Se2 solar cells: a thermodynamic approach," *Thin Solid Films*, vol. 361-362, pp. 338-345, 2000.

[40] W.E. Devaney and R.A. Mickelsen, "Vacuum deposition processes for $CuInSe_2$ and $CuInGaSe_2$ based solar cells," *Solar Cells*, vol. 24, pp. 19-26, 1988.

[41] R.W. Birkmire, L.C. DiNetta, P.G. Lasswell, J.D. Meakin, and J.E. Phillips, "High efficiency $CuInSe_2$ based heterojunction solar cells: Fabrication and results," *Solar Cells*, vol. 16, pp. 419-427, 1986.

[42] L. D. Laude, M. C. Joliet, and C. Antoniadis, "Laser-induced synthesis of thin $CuInSe_2$ films," *Solar Cells*, vol. 16, pp. 199-209, 1986.

[43] M.C. Joliet, C. Antoniadis, R. Andrew, and L.D. Laude, "Laser-induced synthesis of thin $CuInSe_2$ films," *Applied Physics Letters*, vol. 46, pp. 266-267, 1985.

[44] R.D.L. Kristensen, S.N. Sahu, and D.Haneman, "Flash evaporation of $CuInSe_2$ films," *Solar Energy Material*, vol. 17, pp. 329-345, 1988.

[45] N. Romeo, V. Canevari, G. Sberveglieri, and A. Bosio, "Growth of large-grain $CuInSe_2$ thin-films by flash-evaporation and sputtering," *Solar Cells*, vol. 16, pp. 155-164, 1986.

[46] T.F. Ciszek, "Growth and properties of $CuInSe_2$ crystals produced by chemical vapor transport with iodine," *Journal of Crystal Growth*, vol. 70, pp. 405-410, 1984.

[47] C.W. Bates Jr., K.F. Nelson. S.A. Raza. J.B. Mooney. J.M. Recktenwald, L. Macintosh, and R. Lamorcaux, "Spray pyrolysis and heat treatment of $CuInSe_2$ for photovoltaic applications," *Thin Solid Films*, vol. 88, no. 3, pp. 279-283, 1982.

[48] J. Bougnot, S. Duchemin, and M. Savelli, "Chemical Spray Pyrolysis of $CuInSe_2$ Thin Films", *Solar Cells*, vol. 16, pp. 221-236, 1986.

[49] J. Piekoszewski, J.J. Loferski, R. Beualieu, J. Beall, B. Roessler, and J. Shewchun, "RF-Sputtered $CuInSe_2$ Thin Films", *Solar Energy Material*, vol. 2, pp. 363-372, 1980

[50] B. Schumann, A. Tempel, and G. Kuhn, "Epitaxial Layers of CuInSe2", *Solar Cells*, vol. 16, pp. 43-63, 1986.

[51] N. Takenoshita, "Liquid phase epitaxial growth and electrical characterization of $CuInSe_2$," *Solar Cells*, vol. 16, pp. 65-89, 1986.

[52] Y. Ueno, H. Kawai, T. Sugiura, and H. Minoura, "Electrodeposition of $CuInSe_2$ films from a sulphate bath," *Thin Solid Films*, vol. 157, pp. 159-168, 1988.

[53] V.K. Kapur, B.M. Basol, and E.S. Tseng, "Low cost methods for the production of semiconductor films for $CuInSe_2$/CdS solar cells," *Solar Cells*, vol. 21, pp. 65-72, 1987.

[54] V.K. Kapur, A. Bansal, P. Le, and O.I. Asensio, "Non-vacuum processing of $CuIn_{1-x}Ga_xSe_2$ solar cells on rigid and flexible substrates using nanoparticle precursor inks," *Thin Solid Films*, vol. 431-432, pp. 53-57, 2003.

[55] N.G. Dhere, S.R. Ghongadi, M.B. Pandit, A.H. Jahagirdar and D. Scheiman, "CIGS2 thin-film solar cells on flexible foils for space power," *Progress in Photovoltaics: Research and Applications*, vol. 10, pp. 407-416, 2002.

[56] G. Hodes, T. Engelhard, D. Cahen, L.L. Kazmerski, and C.R. Herrington, "Electroplated $CuInS_2$ and $CuInSe_2$ layers: preparation and physical and photovoltaic characterization," *Thin Solid Films*, vol. 128, pp. 93-106, 1985.

[57] B.M. Başol, V.K. Kapur, A. Halani, and C.R. Leidholm, "Cu(In,Ga)Se2 thin films and solar cells prepared by selenization of metallic precursors," *Journal of Vacuum Science and Technology A*, vol. 14, pp. 2251-2256, 1996.

[58] R.A. Mickelson, W.S. Chen, "Polycrystalline thin-film $CuInSe_2$ soalr cells," in *Proceedings of the 16th IEEE Photovoltaic Specialist Conference*, 1982, pp. 781-785.

[59] K. Zweibel, *Harnessing Solar Power: The Photovoltaic Challenge*, New York: Plenum publishing corporation, 1990.

[60] B.J. Stanbery, "Copper indium selenides and related materials for photovoltaic devices," *Critical Reviews in Solid State and Materials Sciences*, vol. 27, pp. 73-117, 2002.

[61] T. Haalboom, T. Gödecke, F. Ernst, M. Rühle, R. Herberholz, H.W. Schock, C. Beilharz, and K.W. Benz, "Phase relation and microstructure in bulk materials and thin films of the ternary

system Cu-In-Se," in *Proceedings of the 11th International Conference on Ternary and Multinary compounds*, 1997, pp. 249-252.

[62] D. Schmid, M. Ruckh, F. Grunwald, and H.W. Schock, "Chalcopyrite/defect chalcopyrite heterojunctions on the basis of CuInSe2," *Journal of Applied Physics*, vol. 73, pp. 2902-2909, 1993.

[63] A. Niemegeers, M. Burgelman, R. Herberholz, U. Rau, D. Hariskos, H.W. Schock, "Model for electronic etansport in Cu(In,Ga)Se2 solar cells," *Progress in Photovoltaics: Research and Applications*, vol. 6, pp. 407-421, 1998.

[64] S.H. Wei, S.B. Zhang, and A. Zunger, "Effects of Ga addition to CuInSe2 on its electronic, structural, and defect properties," *Applied Physics Letters*, vol. 72, pp. 3199-3201, 1998.

[65] P. Migliorato, J.L. Shay, H.M. Kasper, and S. Wagner, "Analysis of the electrical and luminescent properties of $CuInSe_2$," *Journal of Applied Physics*, vol. 46, pp. 1777-1782, 1975.

[66] R. Noufi, R. Axton, C. Herrington, and S.K. Deb, "Electronic properties versus composition of thin films of $CuInSe_2$," *Applied Physics Letters*, vol. 45, pp. 668-670, 1984.

[67] C.J. Kiely, R.C. Pond, G. Kenshole, A. Rockett, "A TEM study of the crystallography and defect structures of single crystal and polycrystalline copper indium diselenide," *Philosophical Magazine A*, vol. 63, no. 6, pp. 1249–1273, 1991.

[68] J.S. Chen, E. Kolawa, C.M. Garland, M.-A. Nicolet, and R.P. Ruiz, "Mocrostructure of polycrystalline CuInSe2/Cd(Zn)S heterojunction solar cells," *Thin Solid Films*, vol. 219, pp. 183–192, 1992.

[69] T. Wada, "Microstructural characterization of high-efficiency Cu(In,Ga)Se_2 solar cells," *Solar Energy Materials and Solar Cells*, vol. 49, pp. 249-260, 1997.

[70] M.I. Alonso, M. Garriga, C.A.D. Rincón, E. Hernández, and M. León, "Optical functions of chalcopyrite CuGaxIn1-xSe2 alloys," *Applied Physics A: Materials Science & Processing*, vol. 74, pp. 659-664, 2002.

[71] N.G. Dhere, "Review: Present status and future prospects of CIGSS thin film solar cells," *Solar Energy Materials and Solar Cells*, vol. 90, pp. 2181-2190, 2006.

[72] R.W. Birkmire and E. Eser, "Polycrystalline thin film solar cells: Present status and future potential," *Annual Review of Materials Research*, vol. 27, pp. 625-653, 1997.

[73] T. Dullweber, O. Lundberg, J. Malmström, M. Bodegård, L. Stolt, U. Rau, H.W. Schock, and J.H. Werner, "Back surface band gap gradings in Cu(In,Ga)Se_2 solar cells," *Thin Solid Films*, vol. 387, pp. 11-13, 2001.

[74] D.J. Schroeder, "Electronic effects of sodium in epitaxial CuIn1-xGaxSe2," *Journal of Applied Physics*, vol. 82, no. 10, pp. 4982-4985, 1997.

[75] R. Klenk, U. Blieske, V. Dieterle, K. Ellmer, S. Fiechter, I. Hengel, A. Jäger-Waldau, T. Kampschulte, Ch. Kaufmann, J. Klaer, M.Ch. Lux-Steiner, D. Braunger, D. Hariskos, M. Ruckh, H.W. Schock, "Properties of $CuInS_2$ thin films grown by a two-step process without H_2S," *Solar Energy Materials and Solar Cells*, vol. 49, pp. 349-356, 1997.

[76] T. Nakada, H. Ohbo, T. Watanabe, H. Nakazawa, M. Matsui, and A. Kunioka, "Improved Cu(In,Ga)(S,Se)$_2$ thin film solar cells by surface sulfurization," *Solar Energy Materials and Solar Cells*, vol. 49, pp. 285-290, 1997.

[77] S.H. Wei, S.B. Zhang, and A. Zunger, "Effects of Na on the electrical and structural properties of CuInSe$_2$," *Journal of Applied Physics*, vol. 85, pp. 7214-7218, 1999.

[78] M.A. Contreras, B. Egaas, P. Dippo, J. Webb, J. Granata, K. Ramnathan, S. Asher, A. Swartzlander and R. Noufi, "On the role of Na and modifications to Cu(ln,Ga)Se$_2$ absorber materials using thin-MF (M=Na, K, Cs) precursor layers," in *Proceedings of 26th IEEE Photovoltaic Specialists Conference*, p. 359, 1997.

[79] D. Braunger, D. Hariskos, S.W. Schock, "Polycrystalline Cu(In,Ga)Se$_2$ solar cells", in *2nd World Conference of Photovoltaic Solar Energy Conversion*, 1998, p. 511

[80] K. L Chopra and S. R. Das, "*Thin Films for Solar Cells*", Plenum press: New York, 1983.

[81] D. Haneman, "Properties and applications of copper indium diselenide", *Critical Reviews in Solid State and Materials Sciences*, vol. 14, pp. 377-413, 1988.

[82] I. Kaur, D. Pandya and K. Chopra, "Growth kinetics and polymorphism of chemically deposited CdS films," *Journal of Electrochemical Society*, vol. 127, pp. 943-948, 1980.

[83] K. Djessas, G. Massé, and M. Ibannaim, "CuInS$_2$ Thin Films for Solar Cell Applications", *Journal of the Electrochemical Society*, vol. 147, pp. 1235-1239, 2000.

[84] D. Schmid, M. Ruckh, and H.W. Schock, "A comprehensive characterization of the interfaces in Mo/CIS/CdS/ZnO solar cell structures," *Solar Energy Materials and Solar Cells*, vol. 41-42, pp. 281-294, 1996.

[85] M.A. Contreras, M.J. Romero, B. To, F. Hasoon, R. Noufi, S. Ward, and K. Ramanathan, "Optimization of CBD CdS process in high-efficiency Cu(In,Ga)Se_2-based solar cells," *Thin Solid Films*, vil. 403-404, pp. 204-211, 2002.

[86] J. Schoenes, K. Kanazawa, and E. Kay, "Band and hopping conduction in high-resistivity ZnO," *Journal of Applied Physics*, vol. 48, pp. 2537-2542, 1977.

[87] G. Neumann, "On the defect structure of zinc-doped zinc oxide," *Physica Status Solidi (b)*, vol. 105, pp. 605-612, 1981

[88] S. Ishizuka, K. Sakurai, A. Yamada, K. Matsubara, P. Fons, K. Iwata, S. Nakamura, Y. Kimura, T. Baba, H. Nakanishi, T. Kojima, and S. Niki, "Fabrication of wide-gap Cu($In_{1-x}Ga_x$)Se_2 thin film solar cells: a study on the correlation of cell performance with highly resistive i-ZnO layer thickness," *Solar Energy Materials and Solar Cells*, vol. 87, pp. 541-548, 2005.

[89] S. Ashour, A.H. Moutinho, R. Matson, and F. Abou-Elfotouh, "Junction formation and characteristics of CdS/$CuInSe_2$/Metal interfaces," *Thin Solid Films*, vol. 226, pp. 129-134, 1993.

[90] S. Raud and M.-A. Nicolet, "Study of the $CuInSe_2$/Mo thin film contact stability," *Thin Solid Films*, vol. 201, pp. 361-371, 1991.

[91] K. Granath, A. Rockett, M. Bodegard, C. Nender, and L. Stolt, "Mechanical Issues of Mo Bacck Contact for Cu(InGa)Se_2", in *Proceedings of the 13th European Photovoltaic Solar Energy Conference*, 1995, p. 1983.

[92] D.W. Hoffman and J.A. Thornton, "Effects of substrate orientation and rotation on internal stresses in sputtered metal films," *Journal of Vacuum Science and Technology*, vol. 16, pp. 134-137, 1979.

[93] Y. Leterrier, "Durability of nanosized oxygen-barrier coatings on polymers," *Progress in Materials Science*, vol. 48, pp. 1-55, 2003.

[94] W.K. Batchelor, I.L. Repins, J. Schaefer, and M.E. Beck, "Impact of substrate roughness on $CuIn_xGa_{1-x}Se_2$ device properties," *Solar Energy Materials and Solar Cells*, vol. 83, pp. 67-80, 2004.

[95] A.A. Kadam, "Preparation of efficient CuInGaSeS/CdS thin-film solar cells by optimizing the molybdenum back contact and using diethyleselenide as selenium precursor." Ph.D. dissertation, University of Central Florida, Orlando, FL, USA, 2006.

[96] M. Benabdi and A.A. Roche "Mechanical properties of thin and thick coatings applied to various substrates. Par 1. An elastic analysis of residual stresses within coating materials," *Journal of Adhesion Science and Technology*, vol. 11, pp. 281-299, 1997.

[97] G.G. Stoney, The tension of metallic films deposited by electrolysis, in *Proceedings of the Royal Society of London*, 1909, vol. 82, pp. 172-175.

[98] W.C. Young, *Roark's Formulas for Stress and Strain*, 6th ed. Texas: McGraw-Hill, 1989.

[99] S. Timoshenko, "Analysis of bi-metal thermostats," *Journal of Optical Society of America*, vol. 11, p. 233, 1925.

[100] L.I. Maissel, R. Glang, Ed., "*Handbook of thin film technology*," New York: McGraw-Hill, 1983.

[101] R.W. Hoffman, "The mechanical properties of thin condensed films," *Physiscs of Thin Films*, vol. 3, p. 211, 1966.

[102] C.A. Klein, "How accurate are Stoney's equation and recent modifications," *Journal of Applied Physics*, vol. 88, no. 9, pp. 5487-5489, 2000.

[103] S.M. Rossnagel and H.R. Kaufman, "Current-voltage relations in magnetrons," *Journal of Vacuum Science and Technology A*, vol. 6, pp. 223-229, 1988.

[104] S.D. Ekpe and S.K. Dew, "Theoretical and experimental determination of the energy flux during magnetron sputter deposition onto an unbiased substrate," *Journal of Vacuum Science and Technology A*, vol. 21, pp. 476-483, 2003.

[105] E.F. Kaeble, *Handbook of X-rays*, New York: McGraw-Hill, 1967.

[106] B.E. Warren, *X-ray Diffraction*, Reading, MA: Addison-Wesley, 1969.

[107] A.S. Reddy, Hyung-Ho Park, V. Sahadeva Reddy, K.V.S. Reddy, N.S. Sarma, S. Kaleemulla, S. Ulhanna, and P.S Reddy, "Effect of sputtering power on the physical properties of dc magnetron sputtered copper oxide thin films," *Materials Chemistry and Physics*, vol. 110, pp. 397-401, 2008.

[108] K. Granath, L. Stold, M. Bodegerd, A. Rockett, and D. Schroeder, in *Proceedings of the 14th European Photovoltaic Solar Energy Conference*, 1997, p. 1278.

[109] R.F. Egerton, *Electron Energy Loss Spectroscopy in the Electron Microscope*, 2nd ed. New York: Plenum, 1996.

[110] K.H. Müller, "Stress and microstructure of sputter-deposited thin films: Molecular dynamics investigations," *Journal of Applied Physics*, vol. 62, pp. 1796-1799, 1987.

[111] M. Itoh, M. Hori, and S. Nadahara, "The origin of stress in sputter-deposited tungsten films for x-ray masks," *Journal of Vacuum Science and Technology B*, vol. 9, pp. 149-153, 1991.

[112] G.M. Turner, "Monte carlo calculations of gas rarefaction in a magnetron sputtering discharge," *Journal of Vacuum Science and Technology A*, vol. 13, pp. 2161-2169.

[113] S. Mahieu, G. Buyle, D. Depla, S. Heirwegh, P. Ghekiere, and R. De Gryse, "Monte Carlo simulation of the transport of atoms in DC magnetron sputtering," *Nuclear Instruments and Methods in Physics Research B*, vol. 243, pp. 313-319, 2006.

[114] I. Blech and U. Cohen, "Effects of humidity on stress in thin silicon dioxide films," *Journal of Applied Physics*, vol. 53, pp.4202-4207, 1982.

[115] H. Windischmann, R.W. Collins and J.M. Cavese, "Effect of hydrogen on the intrinsic stress in ion beam sputtered amorphous silicon film," *Journal of Non-Crystalline Solids*, vol. 85, p. 261, 1986.